Contrib Mineral Petrol (2007) 154:493–517
DOI 10.1007/s00410-007-0205-9

ORIGINAL PAPER

Origin and timing of the post-Variscan gabbro–granite complex of Porto (Western Corsica)

Maria Rosaria Renna · Riccardo Tribuzio · Massimo Tiepolo

Received: 27 July 2006 / Accepted: 3 April 2007 / Published online: 26 April 2007

Abstract The post-Variscan complex of Porto consists of metaluminous to slightly peraluminous A-type biotite granites mingled with gabbro-dioritic rocks, and late dykes with basaltic to trachyandesitic composition. U-Pb zircon dating by LA-ICP-MS on two mafic intrusive samples constrains the time of the gabbro–granite crystallisation at 281 ± 3 Ma and 283 ± 2 Ma. Hornblende ^{40}Ar-^{39}Ar ages from a late trachyandesite dyke date the dyking event at 280 ± 2 Ma, which is within error the U-Pb zircon ages of the intrusives. Biotite granites show variable major and trace element compositions and similar initial ε_{Nd} (–0.3 to +0.9). Whole rock chemistry variations and trace element compositions of plagioclase and allanite indicate that the granites are genetically linked, essentially through fractional crystallisation of feldspars and minor allanite. On the basis of whole-rock chemistry e.g. initial ε_{Nd} +4.9 to +1.7 and trace element clinopyroxene compositions, we have ascertained that the mafic intrusives and basic dykes formed from isotopically depleted mantle source-derived melts with similar trace element signature. These basic melts experienced slightly different evolutionary histories, controlled by fractional crystallisation and crustal contamination, mainly by the acid magma that gave rise to the associated biotite granites, but also by the enclosing older Variscan granitoids. U-Pb zircon data suggest that the Porto complex was affected by hydrothermal fluid circulation at 259 ± 9 Ma.

Keywords Bimodal magmatic association · U-Pb zircon geochronology · Sardinia-Corsica batholith · Variscan orogeny · Laser ablation-ICP-MS · Mineral trace element compositions

Communicated by J. Hoefs.

M. R. Renna (✉) · R. Tribuzio
Dipartimento di Scienze della Terra,
Universitá di Pavia, Via Ferrata 1,
27100 Pavia, Italy
e-mail: renna@crystal.unipv.it

R. Tribuzio · M. Tiepolo
C.N.R. - Istituto di Geoscienze e Georisorse,
Unità di Pavia, Via Ferrata 1,
27100 Pavia, Italy

Introduction

The gabbro–granite complex of Porto includes a large range of rocks varying from gabbros to granites and late mafic dykes. The emplacement of this complex was commonly referred to as the latest ''anorogenic'' stage of the Variscan cycle. Previous studies on the Porto complex (van Tellingen 1955; Vellutini 1975; Platevoet et al. 1988; Platevoet and Bonin 1991; Poitrasson et al. 1995a) distinguished two main types of granite: the *white granite* that forms the main central part of the complex and is intimately associated with gabbroic rocks, forming the so called *gabbro–granite association of Ota*, and the *red Calanche granite* that essentially constitutes the external portion of the Porto complex and was interpreted as a remnant of a ring-dyke emplaced later than the central *gabbro–granite association* (Bonin 1988; van Tellingen et al. 1988). Poitrasson et al. (1995a) conducted a geochemical and isotope study concluding that the two granite types have A-type geochemical affinity but are not genetically related. Renna et al. (2006) gave further information on the origin and the igneous evolution of the gabbroic rocks that form the *gabbro–granite association of Ota*. In particular, these authors showed that Ota basic melts were

derived from a depleted mantle source in relation to a batholith-scale magmatic episode that occurred at about 280 Ma, in response to lithospheric extension subsequent to the Variscan collision.

Previous geochronological investigations of the main Porto rock-types emplacement yielded highly variable ages (ranging from 20 to 280 Ma) and therefore in some cases imprecise. In particular, a low level of confidence is revealed by the high MSWD (mean square weighted deviate = 81) attached to the Rb-Sr whole rock isochron yielding an age of 251 ± 14 Ma (initial $^{87}Sr/^{86}Sr$ = 0.7004 ± 0.0101) for the *red Calanche granite* (van Tellingen et al. 1988). This granite was thus interpreted to post-date the central *gabbro–granite association of Ota*. In addition, the temporal and genetic relations of mafic intrusives and dykes are questionable. On the basis of apatite fission tracks, van Tellingen et al. (1996) dated the emplacement of the Porto mafic dykes at 20–25 Ma. van Tellingen et al. (1996) thus considered the dyking event as related to the opening of the Golfe du Lion.

Many aspects on the magmatic evolution and timing of emplacement of dyke and intrusive rocks of the Porto complex remain poorly defined. In particular, the petrogenesis and geochronology of the rare mafic intrusives (Platevoet et al. 1988) associated with the *red Calanche granite* are unknown. Better-constrained emplacement ages could give new information about the possible petrogenetic relations between mafic intrusives and dykes and between the *white* and *red Calanche granites*. Therefore, to achieve consistent chronological relationships between the different rock-types of the Porto complex, U-Pb zircon dating of two mafic samples mingled with the *white* and the *red Calanche granite* was carried out using laser ablation (LA)-ICP-MS. Furthermore, one ^{40}Ar-^{39}Ar step heating investigation was performed on a hornblende separate from a late dyke. In addition, whole-rock and clinopyroxene major and trace element analyses, coupled with Nd isotope whole-rock determinations, have been obtained on mafic rocks to get a comprehensive overview on the evolution and composition of the basic melts involved in the formation of the Porto complex, and to identify the possible role of the continental crust in the petrogenetic process. New insights into the relations between the *white* and *red Calanche granite* and the evolution of their parental melts were gained through major, trace element and Nd isotope compositions of whole rocks, together with the trace element composition of plagioclase and accessory allanite. As a whole, the geochronological and petrological results obtained have allowed us to provide an accurate relative timing of different mafic and granite products, and to give new information on the origin and evolution of the Porto complex. New U-Pb zircon data also allowed to recognise older component inherited from the country granitoids and to identify a hydrothermal event occurring after the emplacement age. On a broader perspective, the reconstruction of the origin and evolution of the Porto complex can contribute to the geodynamic characterization of the context in which basic and A-type felsic magmatism developed, in the framework of the post-collisional Variscan evolution.

Geological framework

The Corsica batholith is traditionally subdivided into three main magmatic units whose emplacement occurred during the late- to post-collisional phases of the Variscan orogeny, as the result of a discontinuous succession of different short-lived volcanic and plutonic episodes (Paquette et al. 2003; Cocherie et al. 2005). The earliest intrusions, dated at about 340 Ma, are mainly Mg–K rich granitoids with a shoshonitic affinity (Cocherie et al. 1994; Ferré and Leake 2001; Paquette et al. 2003). Calc-alkaline intrusions, largely dominated by low-K hornblende granitoids, came later at about 305 Ma (Cocherie et al. 1994; Tommasini et al. 1995; Paquette et al. 2003). Mafic sequences of tholeiitic affinity and related dyke swarms were then emplaced almost simultaneously with peralkaline to slightly peraluminous A-type granites, between 290 and 280 Ma (Paquette et al. 2003; Cocherie et al. 2005).

The Porto complex of Western Corsica (Fig. 1) is a shallow-level intrusion dominated by granites, which are locally intimately associated with mafic intrusive rocks (Platevoet and Bonin 1991; Renna et al. 2006). The central *gabbro–granite association of Ota* comprises mafic intrusive rocks (gabbros to quartz-diorites) that crop out as disrupted lenses within the *white granite*. The latter is a leucocratic, medium- to coarse-grained and nearly equigranular rock. Towards the contacts with the granite, the largest mafic bodies (up to tens of metres in size) grade to variably shaped small mafic enclaves (up to a couple of metres in size). These textures were interpreted as the result of mingling between magmas with contrasting compositions (Platevoet and Bonin 1991; Renna et al. 2006). Limited hybridisation between basic and acid magmas in the *Ota association* is documented by the development of volumetrically subordinate amphibole-bearing granodiorites to granites close to the mafic enclaves.

The external portion of the Porto complex mainly consists of the so-called *red Calanche granite*. This rock is reddish, equigranular, mostly coarse-grained and richer in K-feldspar than the *white granite*. The *red Calanche granite* commonly contains miarolitic cavities suggesting that the granite was emplaced within a few kilometres of the surface and had reached saturation with respect to H_2O (Bennet 1980; Bennet and Knowles 1983; Lewis and Kilsgaard 1991). Field evidence indicating that the *red*

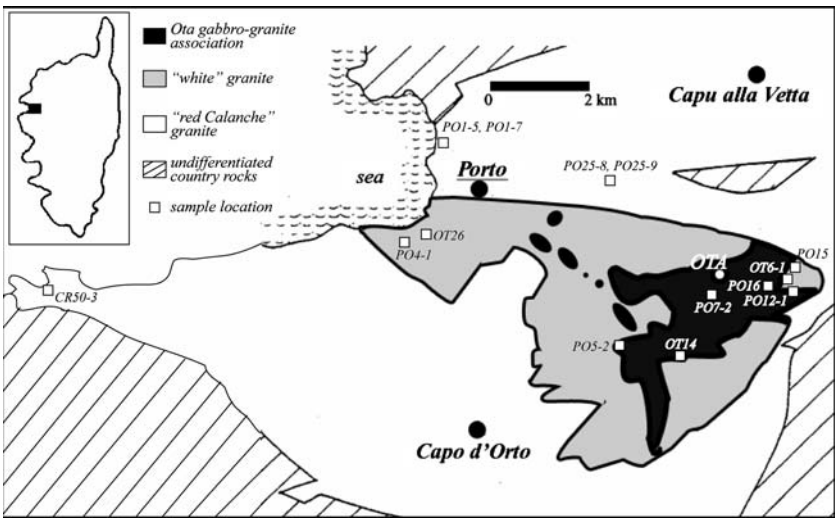

Fig. 1 Schematic geologic map of the Porto Complex (slightly modified after van Tellingen et al. 1988) and location of selected samples

Calanche granite emplaced later than the *white granite* are lacking. In particular, in the south-western sector of the Porto complex, the contact between *white* and *red Calanche granites* is characterised by an hectometre scale layer, intensively altered, with intermediate modal compositions (see also van Tellingen 1955). A gabbroic body showing mingling relations with the *red Calanche granite* crop out at Punta di a Guardiola. The *red Calanche granite* contains in places centimetre-scale mafic enclaves.

The Porto complex has also discordant mafic dykes. In particular, a suite of mafic dykes is well exposed at the Bussaglia beach, North of Porto (see also van Tellingen et al. 1996). Most mafic dykes are up to 10 m thick but typically 1–5 m, and are subvertical and porphyritic, with euhedral plagioclase phenocrysts that usually decrease in number towards the edges of the dyke. The contacts with the host *red Calanche granite* are generally sharp. Nevertheless, some of the dykes show irregular margins with convex-outward lobes that intrude the host rock (Fig. 2), thus indicating that the dyke intrusion occurred when the granite was not completely solidified. *Red Calanche granite* and K-feldspar remnants are observed in places within the mafic dykes. In addition, a few mafic dykes are crosscut by irregular thin K-feldspar rich veins, which are associated with parallel-orientated K-feldspar grains (Renna 2004). This veins most likely represent late magmatic injections segregated out of the host acid melt promoting the crystallisation of new K-feldspar grains in the mafic body. Rare amphibole and biotite rich dykes, with planar contacts, are also present. Only a few mafic dykes crosscut the *Ota association* and commonly show chilled margins against the host rocks.

Fig. 2 Photograph of a mafic dyke showing crenulate margins with convex-outward lobes that intrude the host *red Calanche granite*

The enclosing country rocks of the Porto complex mainly consist of granitoids with calc-alkaline affinity (Vellutini 1975). In particular, the *red Calanche granite* intrudes the Mg–K rich granitoids in the northern and southern sectors, and is in contact with the peralkaline granites of Capu Rossu and Evisa in the south-western and north-eastern ends, respectively (Vellutini 1975; Carmignani et al. 2000). The peralkaline granitic pluton of Evisa has been recently dated at 287 ± 1 Ma by SHRIMP U-Pb zircon geochronology (Cocherie et al. 2005).

Previous geochronological investigations of the Porto intrusive rocks point to an Early Permian age. K-Ar determinations on hornblende and biotite from mafic rocks of the *Ota association* yielded a crystallisation age of 282 ± 10 Ma (Edel et al. 1981). The *white* and *red Calanche granites* were formerly dated by whole-rock Rb-Sr and provided two isochrons of 274 ± 4 and 251 ± 14 Ma, respectively (van Tellingen et al. 1988). For this calculation, however, two samples of *white granite* were excluded. K-Ar biotite ages of 276 ± 4 Ma and 285 ± 5 Ma, and a Rb-Sr whole rock-biotite isochron of 287 ± 6 Ma were also obtained for the *white granite* by van Tellingen et al. (1996). The only available geochronological data for the mafic dykes that crosscut the *red Calanche granite* (van Tellingen et al. 1996) are apatite fission tracks age of 20–25 Ma and K-Ar whole-rock ages ranging from 46 to 141 Ma.

Selected samples

Mafic intrusive rocks

A sample of gabbro (hereafter referred to as Porto-gabbro) mingled with the *red Calanche granite* has been selected for this study. An olivine-bearing gabbro, an olivine-free gabbro and two quartz-diorites from the central *Ota association*, described by Renna et al. (2006), have been also considered. The Porto-gabbro is composed of euhedral plagioclase (~50% by volume), ophitic clinopyroxene (~10%) and anhedral brown amphibole (~35%); ilmenite, biotite, acicular apatite and zircon occur as accessory phases. Plagioclase cores are usually altered into fine-grained aggregates of albite and epidote; plagioclase rims have anorthite contents of 54–45 mol%, within the range displayed by plagioclase rims from the Ota gabbros (Renna 2004). The Mg# [$Mg^{2+}/(Mg^{2+} + Fe^{2+} + Fe^{3+})$] of the clinopyroxene from the Porto-gabbro ranges from 0.75 to 0.71 and is similar to that shown by the clinopyroxene from the Ota gabbros (Renna 2004). U-Pb zircon dating was carried out for the Porto-gabbro and one quartz-diorite from the *Ota association*.

Dykes

Two representative mafic dyke samples were chosen for this study: a medium-grained dolerite (PO1-5) that intrudes the *red Calanche granite* (hereafter referred to as Porto-dolerite) and a porphyritic dyke (PO7-2) that crosscuts the central *Ota association* (hereafter referred to as Ota-dyke). Samples were collected from the central, least-altered portion of the dykes. The Porto-dolerite typically displays a sub-ophitic texture and mostly consists of plagioclase and clinopyroxene; minor amounts of brown amphibole and Fe–Ti oxide phases also occur. The Mg# of clinopyroxene from the Porto-dolerite (0.76–0.71) is similar to that of clinopyroxene from the Ota and Porto gabbros (Renna 2004). The Ota-dyke has rare euhedral plagioclase phenocrysts settled in an aphanitic groundmass, made of plagioclase, clinopyroxene and Fe–Ti-oxide phases; this dyke also contains quartz-ocelli mantled by clinopyroxene. In both rocks, plagioclase is altered into fine-grained aggregates of albite and epidote. In the Ota-dyke, clinopyroxene is commonly replaced by tremolite and chlorite.

One sample of an amphibole and biotite rich dyke (PO1-7) intruding the *red Calanche granite* was selected. It is fine-grained and mainly consists of plagioclase (commonly altered to albite and epidote), biotite and green hornblende. Rare euhedral plagioclase phenocrysts have been locally found. An amphibole separate from dyke PO1-7 has been prepared for ^{40}Ar-^{39}Ar dating.

Biotite granites

Four *white* and two *red Calanche granite* samples have been considered. These include two *white granites* sampled close to the Ota mafic rocks and described by Renna et al. (2006). The *white granites* consist of perthitic K-feldspar (30–40 vol%), quartz (~30 vol%) and plagioclase (20–25 vol%). Remarkably, plagioclase rims have lower anorthite content than cores (9–14 and 14–18 mol%, respectively, Renna 2004). Minor biotite (5–10 vol%) also occurs, mostly as inclusion in quartz and K-feldspar. Common accessory phases are zircon, allanite, Fe–Ti oxide phases and apatite. The *red Calanche granite* differs from the *white granite* in the higher K-feldspar and quartz modal abundances (45–50 and ~35 vol%, respectively), and in the lower amounts of plagioclase (10–15 vol%). Both *white* and *red Calanche granites* are characterised by the common occurrence of granophyric textures, which are recognised as resulting from rapid crystallisation at shallow depth (Barker 1970). In agreement with the occurrence of miarolitic cavities in the *red Calanche granite*, low-pressure plutonic conditions of crystallisation can be thus inferred for the biotite granites. In the *red Calanche granite* plagioclase and biotite are altered into albite + epidote and chlorite, respectively. Metamictization and the presence of high amount of common Pb hampered the achievement of reliable geochronological determinations on zircons from biotite granites (Renna 2004).

Analytical techniques

Eight representative samples were selected for chemical analyses after field and petrographic investigations. Whole-rock major and trace element compositions of these samples were analysed by X-ray fluorescence (XRF) and inductively coupled plasma mass spectrometry (ICP-MS) at the European Union Large Scale Geochemical Facility (Department of Earth Sciences, University of Bristol) and at Activation Laboratories (Ancaster, Ontario). Results and further details are reported in Table 1. Analytical precision and accuracy of XRF and ICP-MS analyses are similar to those reported by Renna et al. (2006).

Six samples from the *Ota association* reported by Renna et al. (2006) were also considered. One of these samples (Ota olivine-gabbro PO5-2) was analysed for rare earth elements (REE) by ICP-MS at both European Union Large Scale Geochemical Facility (Department of Earth Sciences, University of Bristol) and Activation Laboratories, and gave consistent results.

Trace element compositions of clinopyroxene, plagioclase and allanite were determined by laser ablation-inductively coupled plasma-mass spectrometry (LA-ICP-MS) at

Table 1 Whole-rock major and trace element compositions of selected samples

Sample Rock-type	PO5-2[b,c] Ota Ol-G	PO5-2[a] Ota Ol-G	PO16[a,c] Ota Cpx-G	OT14[a,c] Ota Qtz-D	PO12-1[a,c] Ota Qtz-D	CR50-3[b] Porto- gabbro	Sample Rock-type	OT6-1[a,c] W-G	PO15[a,c] W-G	PO4-1[a] W-G	OT26[a] W-G	PO25-8[b] R-G	PO25-9[b] R-G	PO1-5[a] B-D (Porto-dolerite)	PO7-2[b] Tb-D (Ota-dyke)	PO1-7[a] Tr-D
Major elements (wt%)							*Major elements (wt%)*									
SiO_2	48.13	–	50.22	49.44	49.31	49.49	SiO_2	75.44	75.29	74.43	74.22	77.73	76.32	49.01	53.24	60.43
TiO_2	1.64	–	1.72	2.30	2.48	2.24	TiO_2	0.18	0.22	0.21	0.19	0.08	0.08	2.47	2.44	0.97
Al_2O_3	17.53	–	16.07	14.70	14.83	16.24	Al_2O_3	12.76	12.41	13.04	13.04	12.05	11.52	15.05	14.37	16.74
$Fe_2O_3^{tot}$	10.10	–	10.41	11.69	12.55	11.27	$Fe_2O_3^{tot}$	1.52	1.80	1.76	1.61	1.36	1.21	11.51	11.25	5.64
MnO	0.16	–	0.16	0.19	0.20	0.17	MnO	0.02	0.02	0.03	0.03	0.02	0.02	0.17	0.18	0.05
MgO	7.50	–	6.58	5.86	5.21	4.59	MgO	0.19	0.27	0.27	0.30	0.10	0.09	5.85	3.76	3.03
CaO	9.50	–	8.76	8.95	7.69	8.14	CaO	0.58	0.84	0.87	0.88	0.30	0.58	7.81	6.41	3.38
Na_2O	3.43	–	3.46	3.42	3.52	3.70	Na_2O	3.52	3.46	3.94	4.45	3.77	3.41	3.37	3.67	5.57
K_2O	0.52	–	0.89	1.21	1.93	1.29	K_2O	5.33	4.97	4.72	4.61	4.44	4.42	1.58	2.21	3.12
P_2O_5	0.28	–	0.30	0.61	0.53	0.52	P_2O_5	0.04	0.06	0.06	0.07	0.02	0.02	0.52	0.58	0.34
L.O.I	1.52	–	1.01	1.16	1.23	1.88	L.O.I	0.25	0.45	0.53	0.46	0.47	0.98	2.31	2.19	0.52
Total	100.30	–	99.57	99.53	99.48	99.53	Total	99.83	99.78	99.86	99.86	100.34	98.65	99.65	100.30	99.79
Mg#	59.5	–	55.6	49.8	45.1	44.7	Mg#	20.0	22.8	23.1	27.2	12.7	12.8	50.2	39.8	51.5
A/NK							A/NK	1.10	1.12	1.12	1.06	1.09	1.11			
A/CNK							A/CNK	1.01	0.98	0.99	0.94	1.04	1.00			
Trace elements (ppm)							*Trace elements (ppm)*									
V	192	–	174	234	252	211	V	6	12	11	7	< 5	< 5	200	253	83
Ga	18.9	–	19.1	19.7	21.4	22.3	Ga	18.6	17.9	19.8	20.3	22.5	20.0	19.5	22.0	21.6
Sn	1.3	–	2	2	2	10.4	Sn	4	2	8	6	8.2	22.0	3	7.0	2
Rb	15.6	–	25.9	32.3	78.1	28.4	Rb	163	128	208	221	274	255	52.8	95.0	246
Sr	370	–	312	316	265	344	Sr	52.1	77.4	56.1	52.6	11.7	7.80	344	226	482
Ba	134	–	173	321	324	326	Ba	242	291	167	159	51	32	281	366	778
Zr	147	–	154	225	249	259	Zr	122	174	143	124	106	136	270	272	242
Nb	11.7	–	14.5	19.2	16.5	14.9	Nb	23.8	20.9	24.3	23.8	28.2	26.3	23.2	21.1	26.3
Y	28.3	–	28.6	41.9	44.1	40.7	Y	32.8	24.6	44.0	47.4	58.6	54.0	42.0	40.9	22.0
Hf	3.4	–	3	6	8	5.8	Hf	5	7	7	8	5.5	6.0	6	6.0	7
Ta	0.50	–	1.32	1.08	1.02	1.08	Ta	1.61	0.92	1.79	2.36	3.35	2.87	1.37	0.84	1.17
Pb	< 5	–	6	7	12	6	Pb	25	22	22	24	25	12	8	18	8
Th	1.09	–	3.19	2.91	7.09	2.98	Th	22.9	20.6	25.7	21.4	30.5	28.3	3.50	6.13	11.7
U	0.36	–	0.71	0.58	1.68	1.09	U	3.76	2.48	6.14	7.73	8.34	6.34	0.87	2.13	2.11
La	11.5	11.8	17.8	28.9	27.0	25.5	La	56.2	74.3	41.8	34.4	30.1	24.0	28.2	35.0	55.0
Ce	27.1	31.3	40.0	67.6	61.8	55.9	Ce	111	143	87.7	73.6	62.7	53.8	63.9	77.6	101

Table 1 continued

Sample Rock-type	PO5-2[b,c] Ota Ol-G	PO5-2[a] Ota Ol-G	PO16[a,c] Ota Cpx-G	OT14[a,c] Ota Qtz-D	PO12-1[a,c] Ota Qtz-D	CR50-3[b] Porto- gabbro	Sample Rock-type	OT6-1[a,c] W-G	PO15[a,c] W-G	PO4-1[a] W-G	OT26[a] W-G	PO25-8[b] R-G	PO25-9[b] R-G	PO1-5[a] B-D (Porto- dolerite)	PO7-2[b] Tb-D (Ota-dyke)	PO1-7[a] Tr-D
Pr	3.86	4.02	5.36	9.21	8.33	7.49	Pr	12.0	14.5	10.0	8.88	7.51	5.36	8.28	8.09	11.5
Nd	16.3	18.1	22.7	39.9	35.5	29.7	Nd	39.0	46.2	35.0	31.8	28.6	23.5	35.0	35.7	41.7
Sm	4.52	4.68	5.46	9.43	8.49	7.50	Sm	6.90	7.30	7.37	7.15	6.56	6.50	8.35	9.43	7.74
Eu	1.73	1.65	1.73	2.89	2.59	2.44	Eu	0.46	0.57	0.45	0.41	0.13	0.10	2.39	2.57	1.94
Gd	4.71	4.90	5.63	9.35	8.52	7.55	Gd	5.65	5.76	6.83	6.16	6.48	7.52	8.30	9.89	6.35
Tb	0.83	0.77	0.88	1.45	1.33	1.26	Tb	0.88	0.77	1.11	1.03	1.23	1.56	1.31	1.59	0.82
Dy	4.93	4.80	5.31	8.36	7.93	7.27	Dy	5.12	4.31	6.89	6.48	8.57	9.93	7.68	8.97	4.35
Ho	1.00	0.96	1.06	1.70	1.60	1.48	Ho	0.99	0.78	1.43	1.33	1.88	2.10	1.53	1.69	0.77
Er	2.84	2.69	2.94	4.65	4.44	4.19	Er	2.92	2.16	4.25	3.98	6.18	6.45	4.06	4.90	1.98
Tm	0.41	0.38	0.42	0.64	0.64	0.60	Tm	0.45	0.31	0.65	0.64	0.97	1.02	0.58	0.75	0.27
Yb	2.51	2.39	2.60	3.95	3.88	3.68	Yb	2.91	1.99	4.16	4.07	6.56	7.04	3.43	4.71	1.63
Lu	0.40	0.33	0.36	0.57	0.55	0.57	Lu	0.40	0.27	0.59	0.58	1.03	1.06	0.48	0.68	0.22

Ol-G Olivine-bearing gabbro, *Cpx-G* olivine-free gabbro, *Qtz-D* quartz-diorite. *W-G* white granite, *R-G* red Calanche granite, *B-D* basalt dolerite, *Tb-D* basalt-trachyandesite dyke, *Tr-D* trachy-andesite dyke

– Not determined

[a] Whole-rock compositions determined at the European Union Large Scale Geochemical Facility (Department of Earth Sciences, University of Bristol). Major elements, Ba, Ga, Hf, Pb, Sn, Sr, V, Y, Zr were analysed by XRF. REE, U, Th, Nb, Ta were analysed by ICP-MS

[b] Whole-rock compositions determined at the Activation Laboratories (Ancaster, Ontario) by ICP-MS

[c] Whole-rock data are from Renna et al. 2006

L.O.I. loss on ignition. Mg# = 100 × molar Mg/(Mg + Fe)

A/NK, molar ratio of $Al_2O_3/(Na_2O + K_2O)$; A/CNK, molar ratio of $Al_2O_3/(CaO + Na_2O + K_2O)$

C.N.R.—Istituto di Geoscienze e Georisorse, Unità di Pavia. The reader is referred to Tiepolo et al. (2003) and Renna et al. (2006) for analytical set up, reproducibility and accuracy. Quantification of these measurements was based on major element mineral compositions determined by electron microprobe analysis at C.N.R.—Istituto di Geoscienze e Georisorse, Unità di Firenze, and reported in Renna (2004). Trace element mineral compositions are reported in Tables 2, 3 and 4.

Amphibole from the biotite-rich dyke PO1-7 was separated using conventional magnetic technique at the Dipartimento di Scienze della Terra of Università di Pavia. The separate was carefully purified by handpicking under a binocular microscope, cleaned ultrasonically and dried with ultrapure acetone. Amphibole was analysed by the ^{40}Ar-^{39}Ar furnace step heating method at the Nevada Isotope Geochronology Laboratory (University of Nevada, Las Vegas). A detailed description of analytical procedures is given in Reiners et al. (2004). Samples were irradiated at the Nuclear Science Center at Texas A&M University, using Fish Canyon Tuff Sanidine, with an age of 27.9 Ma (Steven et al. 1967; Cebula et al. 1986) as a fluence monitor. Samples analysed by the furnace step heating method utilized a double vacuum resistance furnace similar to the Staudacher et al. (1978) design. Ar isotopic measurements were attained using MAP 215-50 mass spectrometer. The sensitivity of the mass spectrometer was ~6×10^{-17} mol mV^{-1} with the multiplier operated at a gain of 60 over the Faraday. Blanks for furnace analyses averaged 37.15 mV for mass 40 and 0.12 mV for mass 36 at 600°C and 53.08 mV for mass 40 and 0.17 for mass 36 at 1,400°C. Most of the data reduction, as well as age calculations, have been carried out using the Isoplot software (Ludwig 2003). An error in J of 0.5% was used in age calculations. Total gas (integrated) ages are calculated by weighting the amount of ^{39}Ar released, whereas the plateau ages are weighted by the inverse of the variance. All ^{40}Ar-^{39}Ar analytical data (Table 5) are reported at the confidence level of 1σ (standard deviation).

Zircons were separated from the Ota quartz-diorite PO12-1 and the Porto-gabbro CR50-3 using conventional heavy-liquid and magnetic techniques at the C.N.R.—Istituto di Geoscienze e Georisorse, Unità di Pisa. Zircons as much free from inclusions and cracks as possible were selected, mounted in epoxy resin and polished down to 1/4 μm of diamond paste. Zircon structures were characterised by cathodoluminescence (CL) imaging at the Dipartimento di Scienze Mineralogiche e Petrologiche (Università di Torino), using a Cambridge Stereoscan S360 electron microscope with an accelerating voltage of 25 kV. The concentrations of REE in zircon (Table 6) were determined at the C.N.R.-Istituto di Geoscienze e Georisorse, Unità di Pavia, using the same LA-ICP-MS instrument employed for trace element determinations in the other minerals, and mostly under the same operating conditions. The spot size was ~10 μm. NIST 610 and stoichiometric ^{29}Si were taken as external and internal standard, respectively. This LA-ICP-MS was also used to perform in situ U-Pb isotope analyses of zircons on selected samples. Procedures were the same as described in Tiepolo (2003). The laser was operated at a repetition rate of 10 Hz with a pulse energy of about 15 J/cm^2, the spot diameter was ~20μm. Elemental fractionation and mass bias were corrected by external standardisation using zircon 91500 (Wiedenbeck et al. 1995). Accuracy of the data during the analytical run was monitored on zircon 02123 (TIMS U-Pb age of 295 ± 1 Ma, Ketchum et al. 2001) that yielded results within error with the reference value (Tables 7, 8). Time-resolved signal were carefully inspected to detect isotopic heterogeneities within the ablated volume that may be related to radiation-damaged domains, inclusions and cracks, as they tend to give discordant data. Only the isotopically homogeneous intervals of at least 25 s were considered. Data reduction and age calculation were performed using the software package LAMTRACE (developed by S. Jackson initially at Memorial University of Newfoundland and later at Macquarie University, Sydney). In each analytical run, the error related to the reproducibility of the standards was then propagated to all determinations and after this procedure each analysis is retained accurate within the quoted errors (Horstwood et al. 2003). The Isoplot software (Ludwig 2003) was used to calculate and plot the concordant ages from ^{206}Pb/^{238}U and ^{207}Pb/^{235}U ratios. Concordia age values are given at 2σ. Analytical data are compiled in Tables 7 and 8.

Six samples (Table 9) were selected for Nd isotope analyses. Nd isotope analyses were performed at Activation Laboratories (Ancaster, Ontario) on a Finnigan MAT 261 8-collector mass-spectrometer in static mode and normalized to ^{146}Nd/^{144}Nd = 0.7219. Sample powder was dissolved in a HF–HNO_3–HCl mixture. Ten La Jolla Nd-standard runs during the period of work yielded ^{143}Nd/^{144}Nd = 0.511852 ± 5 (2 SD). The Nd isotope results were adjusted to the value of ^{143}Nd/^{144}Nd = 0.511860. On the basis of accuracy of ICP-MS analyses, an error lower than 10% has been estimated for the ^{147}Sm/^{144}Nd (Table 9). Using the error propagation equation reported in Blichert-Toft et al. (1995), uncertainties in the ^{147}Sm/^{144}Nd and ^{143}Nd/^{144}Nd ratios result in an error of the initial ε_{Nd} within 0.1.

Whole rock major and trace element compositions

Mafic intrusive rocks

The Porto-gabbro has Mg# of 44.7 and relatively high Al_2O_3 and TiO_2 contents (Table 1). Compared with the Ota gabbros, the Porto-gabbro has lower Mg#, CaO and higher

Table 2 Trace element clinopyroxene compositions (ppm) obtained by LA-ICP-MS

Sample Rock-type	[a]PO5/2 Ota Ol-G	[a]PO16 Ota Cpx-G	[a]PO12-1 Ota Qtz-D	CR50-3 Porto- gabbro	CR50-3 Porto- gabbro	CR50-3 Porto- gabbro	CR50-3 Porto- gabbro	PO1-5 B-D (Porto-dolerite)	PO1-5 B-D (Porto-dolerite)	PO1-5 B-D (Porto-dolerite)	PO1-5 B-D (Porto-dolerite)
V	595	451	428	442	472	520	372	389	310	451	389
Cr	1,840	1,400	6.7	1,290	47	2,360	940	1,870	298	216	433
Sc	194	132	134	160	168	178	132	110	65	105	117
Ti	13,350	6,350	7,660	7,500	8,340	9,270	5,480	6,730	5,380	6,270	6,940
Sr	29.4	23.0	24.3	14.8	16.0	16.9	13.0	20.2	13.9	25.8	23.5
Ba	0.28	0.29	0.62	0.08	0.24	0.35	0.15	<0.12	0.19	<0.15	<0.12
Zr	70.6	31.4	59.1	56.5	72.2	73.4	37.9	23.8	27.5	37.6	29.9
Nb	0.12	0.09	0.06	0.10	0.15	0.14	0.10	0.05	0.09	0.09	0.06
Y	29.3	26.9	45.9	29.7	36.6	30.9	26.0	20.8	16.0	30.4	26.0
Hf	3.02	1.35	2.62	2.65	3.60	3.37	1.69	1.12	1.11	1.60	1.44
Ta	0.04	0.01	0.01	0.01	0.03	0.02	0.01	0.02	0.01	<0.01	0.01
Th	0.02	0.07	0.26	0.01	0.02	0.03	0.17	0.02	0.02	0.03	0.01
U	0.01	0.04	0.11	0.005	0.02	0.06	0.06	0.01	0.01	0.003	0.01
La	1.88	1.73	3.85	2.75	3.66	2.96	2.70	1.42	1.38	2.62	1.79
Ce	8.78	7.64	13.92	10.6	14.7	12.3	10.3	7.60	8.13	15.4	9.25
Pr	1.86	1.54	2.73	2.16	2.88	2.47	1.93	1.50	1.45	2.97	2.02
Nd	11.9	10.0	16.8	13.9	19.1	16.4	11.9	8.9	8.4	15.7	11.3
Sm	4.33	3.81	5.65	4.68	5.89	5.51	4.17	3.40	2.93	5.16	4.18
Eu	1.58	1.28	1.74	1.77	2.25	1.91	1.28	1.05	0.98	1.49	1.24
Gd	5.69	4.67	8.30	6.10	7.03	5.85	4.51	3.70	3.47	5.86	4.94
Tb	0.91	0.84	1.41	1.03	1.21	1.03	0.74	0.68	0.58	1.12	0.79
Dy	6.24	5.30	9.00	5.95	7.81	7.00	5.40	4.06	3.64	7.35	5.77
Ho	1.20	1.11	1.76	1.31	1.46	1.31	1.04	0.89	0.66	1.26	1.03
Er	3.14	2.89	5.31	3.32	3.96	3.99	2.90	2.61	1.81	3.32	2.88
Tm	0.42	0.37	0.70	0.48	0.54	0.47	0.41	0.32	0.24	0.49	0.39
Yb	2.57	2.50	4.47	2.76	3.83	3.29	2.51	2.36	1.59	3.05	2.58
Lu	0.38	0.36	0.69	0.39	0.57	0.49	0.40	0.31	0.23	0.43	0.35

Ol-G Olivine-gabbro, *Cpx-G* olivine-free gabbro, *Qtz-D*, quartz-diorite, *B-D* basalt dolerite

[a] Clinopyroxene trace element compositions are from Renna et al. (2006)

Table 3 Trace element plagioclase compositions (ppm) obtained by LA-ICP-MS

Sample rock-type	OT6-1 W-G Pl Core	OT6-1 W-G Pl Core	OT6-1 W-G Pl Core	OT6-1 W-G Pl Core	OT6-1 W-G Pl Core	OT6-1 W-G Pl Core	OT6-1 W-G Pl Core	OT6-1 W-G Pl Core	OT6-1 W-G Pl Rim	OT6-1 W-G Pl Rim	OT6-1 W-G Pl Rim	OT26 W-G Pl Core	OT26 W-G Pl Core	OT26 W-G Pl Rim	OT26 W-G Pl Rim	OT26 W-G Pl Rim	OT26 W-G Pl Rim
Ti	50.8	42.6	29.0	58.0	55.6	34.6	35.4	45.6	29.4	35.4	33.5	37.1	52.6	25.8	23.8	21.6	30.7
Rb	2.50	2.65	3.66	4.69	4.51	2.42	2.85	4.93	8.28	12.3	5.89	4.70	9.27	3.42	6.54	3.84	7.26
Sr	150	120	146	189	217	95.5	104	121	24.1	13.2	37.2	165	188	77.2	27.8	45.5	43.7
Ba	101	93.9	96.4	119	141	40.7	34.0	50.9	3.92	2.98	4.62	48.4	113	6.34	1.64	1.98	2.00
Y	0.63	0.13	0.10	0.23	0.15	0.30	0.17	0.13	0.13	0.12	0.10	0.20	0.08	0.07	0.06	0.06	0.07
Pb	31.7	19.7	22.0	20.9	22.1	17.6	14.5	19.2	26.6	40.2	30.5	20.4	22.2	19.1	21.6	16.2	22.5
La	5.91	7.15	4.58	11.7	12.1	5.26	5.63	4.77	2.22	1.74	2.30	5.59	11.5	2.04	1.63	1.36	1.76
Ce	7.83	10.3	7.63	14.0	15.1	7.50	8.20	6.57	3.63	2.90	3.97	8.60	14.5	3.53	3.10	2.52	3.31
Pr	0.59	0.72	0.40	1.20	1.13	0.57	0.63	0.46	0.31	0.25	0.35	0.63	1.06	0.30	0.29	0.20	0.27
Nd	1.25	1.75	0.91	2.36	2.68	1.62	2.15	1.30	0.71	0.69	0.68	1.64	2.04	0.88	0.93	0.71	1.22
Sm	0.34	0.09	0.04	0.26	0.35	0.11	0.18	0.31	<0.01	0.08	0.09	0.13	0.24	0.05	0.06	<0.01	0.08
Eu	0.71	0.60	0.94	1.37	1.24	0.70	0.58	1.05	0.19	0.09	0.24	1.28	1.15	0.57	0.28	0.56	0.35
Gd	<0.02	0.07	0.08	0.07	0.30	<0.04	0.09	<0.06	0.20	<0.02	0.06	<0.02	0.18	<0.01	0.05	<0.01	<0.03
Tb	<0.001	<0.001	<0.001	0.01	<0.004	0.02	0.04	0.004	<0.002	<0.001	<0.003	0.005	<0.01	0.01	<0.001	0.001	0.003
Dy	<0.01	<0.01	0.01	0.09	0.06	0.05	0.02	<0.02	<0.01	<0.01	<0.01	0.04	0.02	0.01	0.03	<0.004	0.01
Ho	0.04	<0.001	0.01	0.01	<0.002	0.01	<0.002	0.01	0.003	<0.002	<0.002	0.01	<0.001	0.001	<0.001	<0.001	<0.001

W-G white granite

Table 4 Trace element allanite compositions (ppm) obtained by LA-ICP-MS

Sample rock-type	OT6-1 W-G	OT6-1 W-G	OT6-1 W-G	OT6-1 W-G	OT26 W-G	OT26 W-G	OT26 W-G
Cr	17.3	22.4	37.6	15.8	165	234	309
Sc	35.5	34.0	60.4	96.1	558	825	1,020
Ti	16,600	17,900	18,800	15,600	13,000	11,500	13,900
Sr	34.8	31.0	299	652	470	478	527
Ba	4.77	4.93	36.8	102	126	118	141
Y	1,560	1,390	2,550	6,410	3,490	4,390	4,010
Pb	197	331	273	422	467	1,290	1,070
Th	5,580	6,770	9,430	15,600	16,300	16,800	15,500
U	37.5	61.8	77.7	140	106	310	755
La	64,400	67,400	64,000	38,600	47,300	39,900	46,300
Ce	110,000	110,000	109,000	74,600	80,900	73,200	77,300
Pr	10,300	9,610	9,990	7,900	8,680	8,170	8,100
Nd	29,800	28,400	29,900	25,800	28,000	29,000	26,200
Sm	2,750	2,540	2,860	3,260	3,200	3,880	3,030
Eu	26.7	27.0	31.4	29.3	32.6	33.2	31.1
Gd	1,580	1,420	1,650	2,040	1,620	1,890	1,560
Tb	142	125	162	265	187	222	197
Dy	571	515	769	1,430	824	943	850
Ho	81.9	75.6	123	238	136	168	148
Er	171	168	341	708	336	448	426
Tm	20.5	20.4	57.8	117	40.6	65.5	66.5
Yb	119	120	431	822	241	462	504
Lu	13.5	14.1	54.0	110	29.9	61.9	70.5

W-G white granite

TiO_2, MnO (Table 1). The chondrite normalised REE profile of the Porto-gabbro shows a steady decrease from LREE to HREE (La_N/ Yb_N = 4.8 for Yb_N = 23) and largely parallels those exhibited by the Ota mafic intrusives (Fig. 3). The Porto-gabbro and Ota quartz-diorites have also similar incompatible trace element patterns (not reported).

Dykes

The Porto-dolerite (PO1-5) and Ota-dyke (PO7-2) fall along the basalt–trachybasalt boundary and in the basaltic trachyandesitic field, respectively, of the total alkali versus silica diagram (TAS, Le Maitre 1989). In particular, the Ota-dyke has lower Mg#, Al_2O_3 and CaO, and higher P_2O_5, MnO, Na_2O and K_2O than the Porto-dolerite (Table 1). The dykes display similar chondrite-normalised REE patterns (Fig. 3), characterised by a gradual decrease from LREE to HREE (La_N/Yb_N = 5.1–5.8 for Yb_N = 21–30), and a weak negative Eu anomaly (Eu_N/Eu^* = 0.81–0.87). The concentrations of Rb, Ba, Th, U, Pb increase from the Porto-dolerite to the Ota-dyke (Table 1).

The amphibole and biotite rich dyke (PO1-7) plots into the trachyandesitic compositional field of the TAS diagram. This trachyandesite differs from the other dykes in the lower TiO_2, CaO, P_2O_5, MnO, and in the higher Al_2O_3, K_2O and Na_2O (Table 1). The chondrite-normalised REE profile (Fig. 3) is characterised by a marked decrease from LREE to HREE (La_N/Yb_N = 23.3 for Yb_N = 10) and a weak negative Eu anomaly (Eu_N/Eu^* = 0.84). The trachyandesite shows higher LREE, Rb, Ba, Th, Sr and lower HREE and Y than mafic dykes (Table 1).

Biotite granites

The biotite granites range from 74.2 to 77.7 wt% SiO_2, with the highest values pertaining to the *red Calanche granites*. *White granites* have higher TiO_2, K_2O, P_2O_5, Al_2O_3, CaO, Fe_2O_3 and Mg# than the *red Calanche granites* (Table 1). As a whole, the biotite granites vary from metaluminous to slightly peraluminous, with molar $Al_2O_3/CaO + Na_2O + K_2O$ values ranging from 0.94 to 1.04 (Table 1).

The chondrite normalised REE patterns of the *white granite* (Fig. 4) display marked LREE enrichment and weak HREE depletion relative to MREE (La_N/Sm_N = 3.0–6.4; Gd_N/Lu_N = 1.3–2.6), and a marked negative Eu anomaly (Eu_N/Eu^* = 0.19–0.27). The *red Calanche granite* is less LREE enriched (La_N/Sm_N = 2.3–2.9) and have nearly flat HREE (Gd_N/Lu_N = 0.78–0.88) at about 40 times chondrite; the negative Eu anomaly is abrupt

Table 5 ^{40}Ar–^{39}Ar analysis of hornblende separate from the trachyandesite dyke PO1-7

Step	T (C)	t (min)	^{36}Ar	^{37}Ar	^{38}Ar	^{39}Ar	^{40}Ar	$\%^{40}Ar^*$	% ^{39}Ar rlsd	Ca/K	$^{40}Ar^*/^{39}ArK$	Age (Ma)	1σ
PO 1-7, amphibole, 8.98 mg, J = 0.001607 ± 0.82%													
4 amu discrimination = 1.01558 ± 0.20%, 40/39 K = 0.0001 ± 100.0%, 36/37Ca = 0.000288 ± 4.09%, 39/37Ca = 0.00071 ± 3.30%													
1	750	12	1.989	0.608	0.643	4.303	992.481	41.8	3.2	1.495	96.791	260.82	2.49
2	850	12	1.691	0.811	0.735	7.512	1156.10	65.2	5.5	1.142	100.591	270.33	2.45
3	950	12	0.544	2.318	0.823	8.809	1059.72	85.4	6.5	2.785	102.744	275.69	2.26
4	990	12	0.407	7.045	1.482	9.215	1057.06	89.3	6.8	8.105	102.638	275.43	2.22
5	1,020	12	0.433	18.911	3.583	14.155	1585.24	92.7	10.4	14.190	104.336	279.65	2.25
6	1,050	12	0.412	30.044	5.684	20.795	2261.16	95.3	15.3	15.350	104.320	279.61	2.25
7	1,070	12	0.237	21.633	4.148	15.341	1643.96	96.5	11.3	14.981	103.968	278.73	2.24
8	1,095	12	0.217	22.244	4.151	15.100	1614.98	96.8	11.1	15.653	104.119	279.11	2.25
9	1,120	12	0.166	19.339	3.512	12.247	1311.74	97.8	9.0	16.784	105.000	281.30	2.26
10	1,140	12	0.110	12.349	2.182	7.557	810.760	98.1	5.6	17.372	105.134	281.63	2.28
11	1,160	12	0.090	7.060	1.247	4.231	457.754	97.4	3.1	17.741	104.522	280.11	2.25
12	1,180	12	0.075	5.034	0.916	2.942	322.070	97.4	2.2	18.195	105.033	281.38	2.33
13	1,210	12	0.104	6.080	1.141	3.440	382.585	95.6	2.5	18.798	105.244	281.90	2.28
14	1,250	12	0.130	8.143	1.593	4.705	516.214	95.5	3.5	18.405	104.144	279.17	2.45
15	1,295	12	0.126	0.432	1.295	3.509	401.450	94.3	2.6	1.303	106.833	285.84	2.32
16	1,400	12	0.130	3.455	0.715	1.832	227.285	96.3	1.4	20.066	111.974	298.51	2.56
								Cumulative $\%^{39}Ar$ rlsd = 100.0			Total gas age =	278.59	2.26
											Plateau age =	279.98	2.36
											steps (5–11)		
											Isochron age =	280.1	2.3
											steps (5–14)		

Note Isotope beams in mV, rlsd = released, error in age includes J error, all errors 1σ

(^{36}Ar through ^{40}Ar are measured beam intensities, corrected for decay for the age calculations)

(Eu_N/Eu^* = 0.04–0.06). Remarkably, LREE, Ba and Sr contents decrease from the *white* to the *red Calanche granites*. Conversely, the concentrations of HREE, Y, Rb and the extent of Eu negative anomaly increase (Table 1).

The Porto biotite granites display trace element characteristics of A-type granites, as defined by Whalen et al. (1987), in agreement with the study of Poitrasson et al. (1995a). For instance, they have high Ga/Al ratios and elevated contents of Zr, Nb, Ce and Y (Fig. 5). Similar geochemical compositions have been reported for other A-type biotite granites from the Corsica batholith (e.g. Tana Peloso Poitrasson et al. 1994).

Mineral trace element compositions

Clinopyroxene from mafic rocks

The chondrite-normalised incompatible trace element profiles of clinopyroxenes from the Porto-gabbro are broadly similar in shape to those of clinopyroxene from the Ota mafic intrusive sequence (Fig. 6). They show Ba, Th, U, Nb, Ta and Sr depletion relative to LREE. In addition, MREE and HREE are enriched over LREE, Zr, and Hf. The incompatible trace element patterns highlight also an enrichment of U relative to Th, Nb and Ba. In particular, U and Th abundances exhibit a wide compositional range (see also Table 2). Clinopyroxene from the Porto-gabbro shows extremely variable Cr contents, which range from 20 to 2,360 ppm. Sc and V vary in the ranges 132–178 and 372–520 ppm, respectively.

The incompatible trace element patterns of clinopyroxene from the Porto-dolerite mostly parallel that of the clinopyroxene from the Ota mafic intrusives (Fig. 6). The clinopyroxene from the Porto-dolerite has very low concentrations of Ba, Th and U (Table 2). Cr in clinopyroxene from the Porto-dolerite shows a high variability (216–1,870 ppm). Sc and V concentrations are 65–117 and 310–451 ppm, respectively.

Plagioclase and allanite from white granites (samples OT6-1 and OT26)

Plagioclases from the two samples have similar REE, Pb, Rb and Ti concentrations (Table 3). Their chondrite-normalised incompatible trace element pattern (Fig. 7)

Table 6 Trace element zircon compositions (ppm) obtained by LA-ICP-MS

Sample	PO12-1	PO12-1	PO12-1	PO12-1	PO12-1	PO12-1	PO12-1	PO12-1	PO12-1
Rock-type	Ota Qtz-D	Ota Qtz-D	Ota Qtz-D	Ota Qtz-D	Ota Qtz-D	Ota Qtz-D	Ota Qtz-D	Ota Qtz-D	Ota Qtz-D
Zircon	Elongate	Elongate	Elongate	Elongate	Elongate	Elongate	Elongate	Stubby	Stubby
Y	3,620	4,980	1,450	5,040	549	4,350	3,860	7,470	3,980
La	0.15	0.47	0.26	0.35	0.05	0.22	0.24	63.0	29.9
Ce	21.9	35.8	6.00	30.0	3.25	49.5	32.1	319	168
Pr	0.92	1.52	0.18	1.14	0.09	0.45	0.84	41.4	9.20
Nd	11.9	18.7	1.91	16.8	0.516	6.28	10.8	194	45.8
Sm	16.8	28.2	4.51	26.1	1.23	14.7	15.7	95.8	22.5
Eu	5.30	11.0	1.32	8.82	0.61	5.48	6.62	3.04	2.41
Gd	73.7	107	15.2	99.9	7.57	71.0	61.4	148	75.8
Tb	27.4	36.1	6.85	33.6	2.61	25.7	20.4	50.2	27.9
Dy	330	368	82.4	362	30.5	315	230	558	332
Ho	126	126	33.6	120	13.4	125	84.2	182	127
Er	554	458	162	455	65.8	556	351	748	542
Tm	131	102	41.0	95.0	16.6	135	83.0	167	115
Yb	1,220	915	403	899	168	1,420	785	1,410	1,050
Lu	181	136	72.7	129	32.1	233	120	199	170

Sample	CR50-3	CR50-3	CR50-3	CR50-3	CR50-3	CR50-3	CR50-3	CR50-3	CR50-3	CR50-3	CR50-3	CR50-3	CR50-3
Rock-type	Porto-gabbro	Porto-gabbro	Porto-gabbro	Porto-gabbro	Porto-gabbro	Porto-gabbro	Porto-gabbro	Porto-gabbro	Porto-gabbro	Porto-gabbro	Porto-gabbro	Porto-gabbro	Porto-gabbro
Zircon	Elongate	Elongate	Elongate	Elongate	Elongate	Elongate	Elongate	Elongate	Elongate	Stubby	Stubby	Stubby	
Y	9,250	11,400	11,200	5,740	7,130	9,290	4,890	13,900	12,400	7,870	3,890	7,870	4,950
La	0.15	0.28	0.36	0.11	0.17	0.08	0.10	0.37	0.42	0.28	14.9	31.7	9.70
Ce	74.4	100.3	117.0	35.7	44.5	92.2	26.0	134	74.5	61.3	79.4	267	163
Pr	1.68	1.59	1.95	1.16	1.10	1.41	0.80	2.80	2.04	1.29	3.98	32.6	12.9
Nd	28.1	26.7	34.4	18.5	17.8	24.9	14.0	45.3	30.0	17.2	23.4	176	72.0
Sm	54.6	53.9	65.2	35.7	37.1	48.8	26.7	89.6	58.0	36.0	21.0	125	48.8
Eu	9.21	9.20	11.1	8.53	7.62	8.75	7.07	16.2	13.2	6.64	3.16	15.4	4.73
Gd	248	272	278	144	160	242	103	411	266	172	85.0	213	90.5
Tb	94.2	106	99.2	49.0	57.0	92.2	36.6	148	94.4	66.8	30.6	69.6	28.7
Dy	1,100	1,230	1,130	557	681	1,120	387	1,510	1,140	814	366	637	297
Ho	388	436	381	202	249	409	139	500	393	295	132	194	105
Er	1,580	1,700	1,460	789	998	1,680	566	1,870	1,600	1,250	552	749	433
Tm	306	331	291	162	202	333	119	382	357	260	116	156	96
Yb	2,480	2,710	2,470	1,470	1,860	2,890	1,060	3,230	3,300	2,240	1,030	1,440	916
Lu	379	415	388	249	296	426	169	501	534	357	176	241	164

Qtz-D quartz-diorite

displays a strong LREE enrichment (La_N/Nd_N = 2.8–10.9) relative to MREE, HREE and Y, and a marked positive Eu anomaly. In addition, Rb and Ti are strongly depleted relative to Pb (by one order of magnitude) and Sr (by two orders of magnitude), respectively. In both samples, plagioclase shows a high variability of Ba values. In particular, Ba decreases by about two orders of magnitude from core to rim. The low-Ba plagioclase rims are also characterised by slightly lower Sr and Eu concentrations, and a less marked LREE enrichment than high-Ba plagioclase (Table 3). Troughs for Ba can be explained by the late crystallisation of K-feldspar, which is characterised by high Ba concentrations (up to 1,590 ppm, Renna 2004).

Allanite from the two selected *white granites* has REE concentrations (Table 4), comparable with those of other allanites from Corsican granitoids (Poitrasson 2002). Its chondrite-normalised REE profile (Fig. 8) is characterised by a marked enrichment of LREE relative to MREE (La_N/Sm_N = 6.5–16.6) and an abrupt negative Eu anomaly (Eu_N/Eu^* = 0.03–0.04). The HREE are strongly to slightly

Table 7 LA-ICP-MS U-Pb analysis of zircons from sample PO12-1 (Ota quartz-diorite) and zircon standard 02123

Zircon	$^{207}Pb/^{235}U$	1σ	$^{206}Pb/^{238}U$	1σ	Apparent ages					
					Concordant ages	2σ	$^{207}Pb/^{235}U$	2σ	$^{206}Pb/^{238}U$	2σ
Stubby zircons										
Zrn 03	0.320	0.011	0.039	0.001			282	35	246	20
Zrn 05	0.444	0.016	0.049	0.001			373	44	311	25
Zrn 06	0.310	0.012	0.044	0.001	277	11	274	36	278	22
Zrn 11	0.993	0.028	0.049	0.001			700	56	306	20
Zrn 11b	1.047	0.036	0.051	0.001			728	71	318	24
Zrn 23	0.447	0.014	0.048	0.001			375	38	304	21
Zrn 25	0.313	0.010	0.044	0.001	274	9	277	30	275	22
Zrn 30	0.615	0.019	0.048	0.001			487	48	304	21
Zrn 41	0.252	0.004	0.038	0.001			228	13	237	18
Eongate zircons										
Zrn 01	0.431	0.020	0.046	0.001			364	57	289	28
Zrn 02	0.344	0.017	0.047	0.001	297	13	300	52	297	27
Zrn 04	0.348	0.016	0.044	0.001			303	49	278	24
Zrn 07	0.315	0.010	0.044	0.001	279	10	278	32	279	21
Zrn 08	0.322	0.012	0.045	0.001	283	10	284	36	283	21
Zrn 09	0.321	0.011	0.044	0.001	279	11	283	33	279	21
Zrn 10	0.315	0.013	0.044	0.001	279	11	278	39	279	22
Zrn 12	0.550	0.013	0.048	0.001			445	35	302	20
Zrn 13	1.127	0.033	0.054	0.001			767	63	337	23
Zrn 14	0.326	0.006	0.045	0.001	287	10	286	19	285	23
Zrn 15*	0.611	0.015	0.048	0.001			484	39	305	22
Zrn 16	0.641	0.013	0.047	0.001			503	33	299	19
Zrn 17*	0.317	0.007	0.044	0.001	280	10	280	21	278	23
Zrn 19	0.334	0.007	0.047	0.001	293	10	293	20	295	23
Zrn 20	0.299	0.010	0.042	0.001	265	10	266	31	265	21
Zrn 21	0.611	0.023	0.046	0.001			484	57	293	22
Zrn 22*	0.316	0.013	0.044	0.001	276	12	279	40	276	24
Zrn 22B	0.361	0.011	0.047	0.001			279	34	291	20
Zrn 24	0.321	0.010	0.043	0.001	274	9	283	32	274	18
Zrn 26	0.441	0.016	0.048	0.001			371	45	299	22
Zrn 27	0.331	0.015	0.045	0.001	282	11	290	45	282	23
Zrn 31*	0.362	0.012	0.047	0.001			313	37	293	22
Zrn 32	0.432	0.019	0.046	0.001			364	54	287	24
Zrn 33	0.555	0.017	0.049	0.001			448	44	305	24
Zrn 34B	0.366	0.007	0.046	0.001			317	21	288	21
Zrn 39	0.351	0.008	0.045	0.001			306	24	282	22
Zrn 40	0.449	0.011	0.046	0.001			377	32	290	24
Zrn 42	0.392	0.010	0.047	0.001			336	30	296	24
02123	0.356	0.013	0.054	0.004	296	13	309	40	338	98

*low luminescent core in elongate zircon

depleted relative to MREE (Gd_N/Lu_N = 2.3–14.5). The lowest HREE (and Y) concentrations correspond to the highest LREE amounts. Uranium and Th contents are high and cover a wide range of values (38–755 and 5,580–16,800 ppm, respectively). Strontium concentrations range between 31 and 652 ppm. Allanite from the *white granite* OT6-1 has lower Pb, Ba, Cr and Sc, and higher Ti than allanite from the *white granite* OT26 (Table 4).

Table 8 LA-ICP-MS U-Pb analysis of zircons from sample CR50-3 (Porto-gabbro) and zircon standard 02123

Zircon	$^{207}Pb/^{235}U$	1σ	$^{206}Pb/^{238}U$	1σ	Apparent ages					
					Concordant ages	2σ	$^{207}Pb/^{235}U$	2σ	$^{206}Pb/^{238}U$	2σ
Stubby zircons										
Zrn0	0.318	0.014	0.048	0.001			280	43	299	15
Zrn06	0.141	0.002	0.009	0.000			134	7	55	4
Zrn17	0.479	0.015	0.050	0.001			398	41	312	31
Zrn19	0.271	0.008	0.034	0.001			243	26	216	21
Zrn31[a]	0.367	0.008	0.050	0.001	317	12	317	25	317	29
Zrn42[a]	0.362	0.009	0.050	0.001	312	12	313	26	312	23
Elongate zircons										
Zrn01	0.328	0.006	0.045	0.001	289	8	288	18	287	23
Zrn02a	0.311	0.005	0.044	0.001	275	7	275	15	275	21
Zrn02b	0.330	0.005	0.046	0.001	289	6	290	16	290	23
Zrn03	0.318	0.007	0.045	0.001	280	10	280	21	281	24
Zrn04	0.332	0.008	0.046	0.001	290	11	291	24	289	25
Zrn07	0.317	0.006	0.044	0.001	280	9	280	17	278	22
Zrn09*	0.343	0.009	0.039	0.001			299	26	249	18
Zrn10	0.327	0.008	0.040	0.001			287	25	255	18
Zrn11	0.335	0.006	0.047	0.001	290	7	293	18	295	25
Zrn12	0.290	0.006	0.041	0.001	259	9	258	18	261	21
Zrn13	0.357	0.011	0.045	0.001			310	34	283	28
Zrn14	0.383	0.012	0.047	0.001			329	34	294	29
Zrn15	0.310	0.010	0.043	0.001	274	15	274	32	273	30
Zrn18	0.406	0.014	0.046	0.001			346	40	287	28
Zrn20	0.334	0.011	0.043	0.001			292	35	268	27
Zrn21	0.352	0.013	0.044	0.001			306	39	277	28
Zrn22	0.330	0.010	0.046	0.001	287	15	290	32	288	31
Zrn23	0.316	0.010	0.044	0.001	276	15	279	31	276	30
Zrn24*	0.317	0.010	0.044	0.001	277	14	280	31	277	29
Zrn26	0.323	0.013	0.050	0.000			285	40	313	12
Zrn27	0.315	0.012	0.044	0.001	282	6	278	37	280	18
Zrn28	0.336	0.013	0.046	0.001	288	8	294	40	290	17
Zrn29	0.292	0.014	0.045	0.001			260	45	284	17
Zrn33	0.555	0.024	0.049	0.001			448	63	307	17
Zrn34	0.277	0.016	0.044	0.001			248	51	279	20
Zrn35a	0.311	0.015	0.043	0.001	272	10	275	45	272	21
Zrn35b	0.314	0.012	0.044	0.001	280	7	277	36	279	18
Zrn36	0.331	0.007	0.046	0.001	289	11	290	22	293	24
Zrn38	0.353	0.010	0.044	0.001			307	30	275	20
Zrn39	0.791	0.031	0.048	0.001			592	71	303	28
Zrn40a	0.315	0.007	0.044	0.001	278	11	278	22	280	24
Zrn40b	0.312	0.010	0.042	0.001	269	10	276	31	267	21
Zrn41	0.329	0.008	0.045	0.001	283	10	289	24	281	21
Zrn43	0.331	0.008	0.046	0.001	291	12	291	24	291	24
Zrn46*	0.329	0.008	0.045	0.001			289	23	283	24
02123	0.345	0.009	0.047	0.001	297	11	301	28	296	22

Younger elongate zircon is reported in italic

[a] Inherited core in stubby zircon

*Low luminescent core in elongate zircon

Table 9 Nd isotope compositions of selected samples. Ol-G, olivine-bearing gabbro; Cpx-G, olivine-free gabbro; Qtz-D, quartz-diorite; Gr, granodiorite; Bt-G, biotite-bearing granite; B-D, basalt dolerite; Tr-D, trachyandesite dyke; W-G, white granite; R-G, red Calanche granite

Sample	rock-type	$^{143}Nd/^{144}Nd \pm$ 2 SE	$^{147}Sm/^{144}Nd$	$^{143}Nd/^{144}Nd_{(282Ma)}$	ε_{Nd}	ε_{Nd} (282 Ma)
PO5/2[a]	Ota Ol-G	0.512813 ± 6	0.156	0.512525 ± 6	+3.4	+4.9 ± 0.1
PO16[a,c]	Ota Cpx-G	0.512673 ± 4	0.150	0.512396 ± 4	+0.7	+2.4 ± 0.1
PO12-1[a,c]	Ota Qtz-D	0.512650 ± 3	0.145	0.512383 ± 4	+0.2	+2.1 ± 0.1
CR50-3[b]	Porto-gabbro	0.512645 ± 5	0.153	0.512363 ± 5	+0.1	+1.7 ± 0.1
PO1-5[a]	B-D (Porto-dolerite)	0.512689 ± 3	0.144	0.512422 ± 4	+1.0	+2.9 ± 0.1
PO1-7[a]	Tr-D	0.512378 ± 3	0.112	0.512171 ± 3	–5.1	–2.0 ± 0.1
OT6-1[a, c]	W-G	0.512492 ± 3	0.107	0.512294 ± 3	–2.8	+0.4 ± 0.1
OT26[a]	W-G	0.512513 ± 5	0.136	0.512262 ± 5	–2.4	–0.2 ± 0.1
PO25-8[b]	R-G	0.512579 ± 3	0.139	0.512323 ± 4	–1.2	+0.9 ± 0.1

2 SE is the uncertainty on measured $^{143}Nd/^{144}Nd$ (internal precision)

[a] $^{147}Sm/^{144}Nd$ calculated on the basis of Sm-Nd obtained by ICP-MS at the European Union Large Scale Geochemical Facility (Department of Earth Sciences, University of Bristol) (see Table 1)

[b] $^{147}Sm/^{144}Nd$ calculated on the basis of Sm-Nd obtained by ICP-MS at at the Activation Laboratories (Ancaster, Ontario) (see Table 1)

[c] $^{143}Nd/^{144}Nd$ values are from Renna et al. 2006

Analytical error on $^{147}Sm/^{144}Nd$ value is ± 10%

The assessment of errors on calculated $^{143}Nd/^{144}Nd$ ratios and corresponding ε values was done using the error propagation equation reported in Blichert-Toft et al. 1995

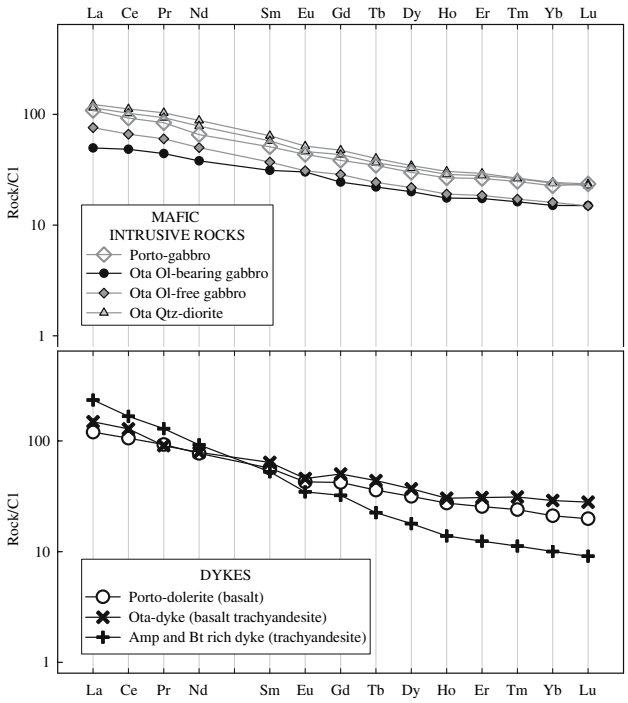

Fig. 3 Whole-rock REE compositions of mafic intrusive rocks and dykes, normalised to C1 chondrite (Anders and Ebihara 1982). The compositions of Ota olive-gabbro PO5-2 are the average of duplicated analyses

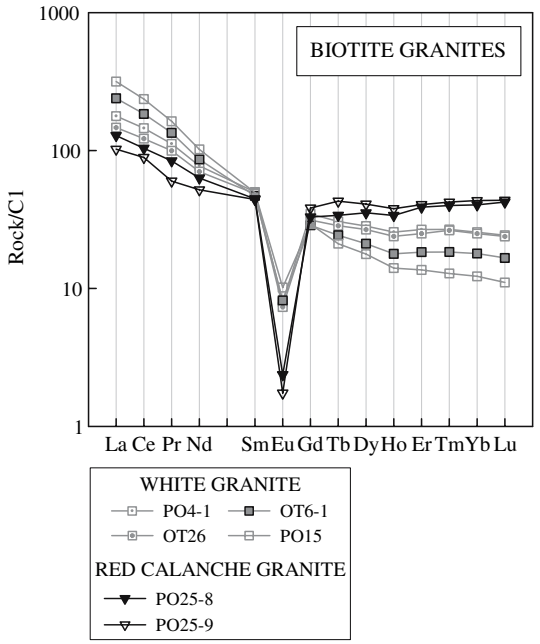

Fig. 4 Whole-rock REE compositions of biotite granites, normalised to C1 chondrite (Anders and Ebihara 1982)

^{40}Ar-^{39}Ar Geochronology

Furnace step heating of hornblende separate from the trachyandesite dyke PO1-7 revealed a nearly flat age spectrum (Fig. 9a; Table 5). A plateau age of 280 ± 2 Ma (1σ) is defined by steps 5–11 (constituting 66% of the total ^{39}Ar released, Fig. 9a). The first four and final five steps are not concordant with the plateau step ages within analytical uncertainties, thus they are rejected in the plateau age estimation. An indistinguishable isochron age of 280 ± 2 Ma (1σ) is defined by steps 5–14 and represents a larger

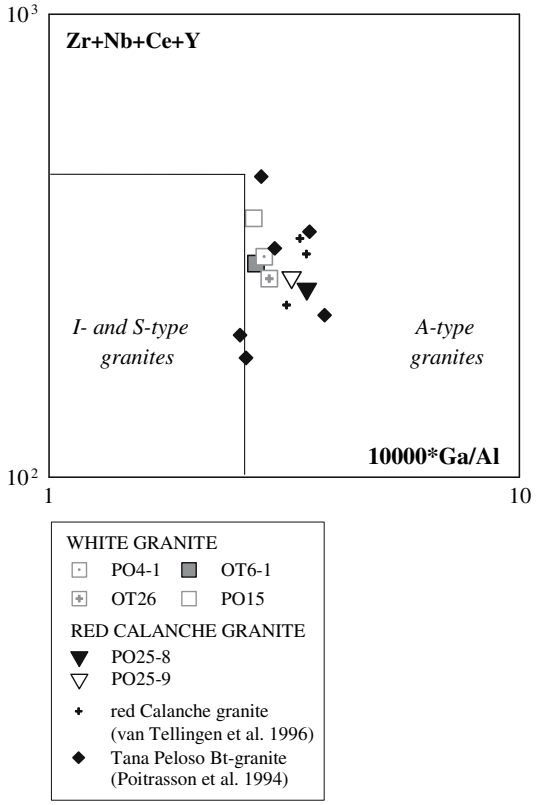

Fig. 5 (Zr+Nb+Ce+Y) versus 10,000*Ga/Al discriminant diagram for A-type granites (Whalen et al. 1987) relative to Porto biotite granites. The compositions of Porto *red Calanche granite* (van Tellingen et al. 1996) and Tana Peloso biotite granite (Poitrasson et al. 1994) are also reported for comparative purposes

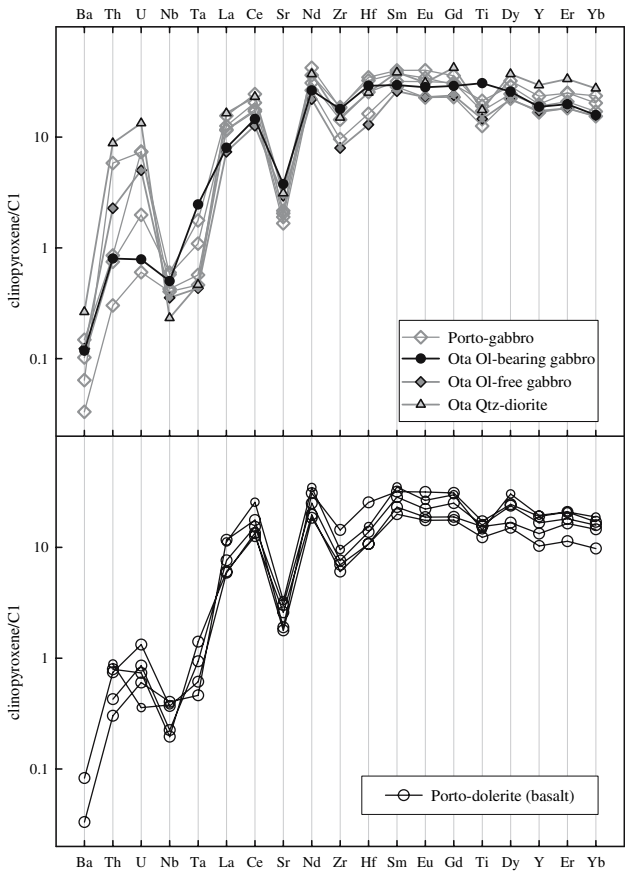

Fig. 6 Incompatible trace element compositions of clinopyroxenes from mafic rocks, normalised to C1 chondrite (Anders and Ebihara 1982)

fraction of the total gas released (79% of the total ^{39}Ar released, Fig. 9b). The isochron also shows that this sample does not have excess argon. Both plateau and isochron ages are indistinguishable from the total gas age of 279 ± 2 Ma (1σ). The isochron age of 280 ± 2 Ma (1σ) is the most reliable crystallisation age for the selected dyke as it defines the isotopic composition of the initial argon in the sample. We propose that the fission track apatite ages of 20–25 Ma found by van Tellingen et al. (1996) reflects an episode of crustal exhumation. The regional distribution of apatite fission-track early to middle Miocene ages well document this episode of crustal exhumation in northern Corsica (Cavazza et al. 2001; Zarki-Janki et al. 2004; Fellin et al. 2005).

U-Pb zircon geochronology and trace element signature of zircon

Zircon from the Ota quartz-diorite

Ota quartz-diorite contains a zircon population that is dominated by elongate to needle-shaped colourless to pale pink crystals (70–200 μm in length and up to 50 μm wide; Fig. 10). These zircons are commonly cracked and locally show tiny K-feldspar inclusions in their cores. Cathodoluminescence (CL) images reveal that these zircons are frequently characterised by oscillatory growth zoning that, however, does not define a regular pattern. Small cores with low luminescence, unzoned or faintly zoned, have been locally found (e.g. zircon grains 15, 17, 22 and 31). These low-luminescent cores are truncated by a thin finely zoned rim (Zrn15 and 17, Fig. 10). Rare stubby, mainly euhedral crystals, dark pink to brownish in colour, are also present (50–150 μm in length and 50–100 μm wide; e.g. Zrn25 and 41, Fig. 10). Cathodoluminescence imaging commonly shows inner structures characterised by regular oscillatory zoning (e.g. Zrn25, Fig. 10) typical of zircons of magmatic origin. Apatite needles inclusions and dark CL domains, commonly ascribed to radiation-damaged zircon (Corfu et al. 2003 and references therein), are frequent (e.g., Zrn 41, Fig. 10).

The representative REE composition of both elongate and stubby zircon fractions, normalised to C1-chondrite, is reported in Fig. 11. The REE pattern of elongate zircons

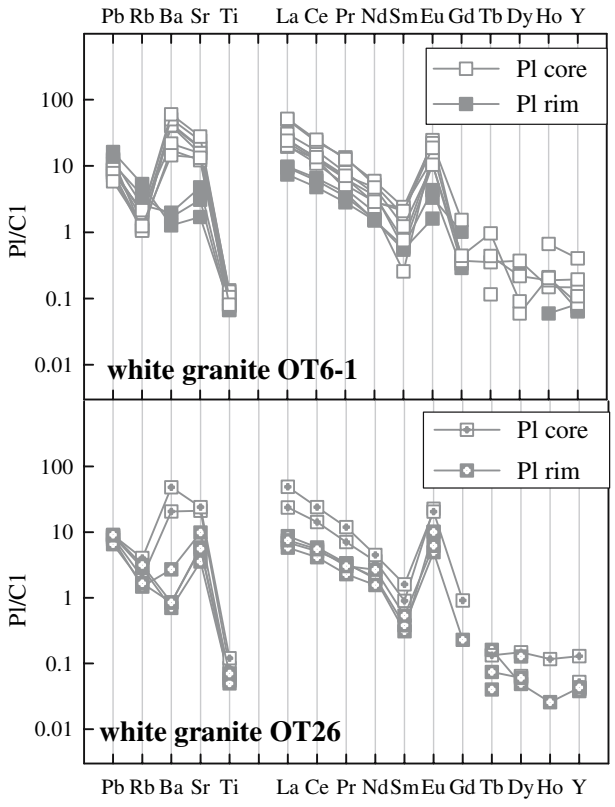

Fig. 7 Incompatible trace element compositions of plagioclases from *white granite*, normalised to C1 chondrite (Anders and Ebihara 1982)

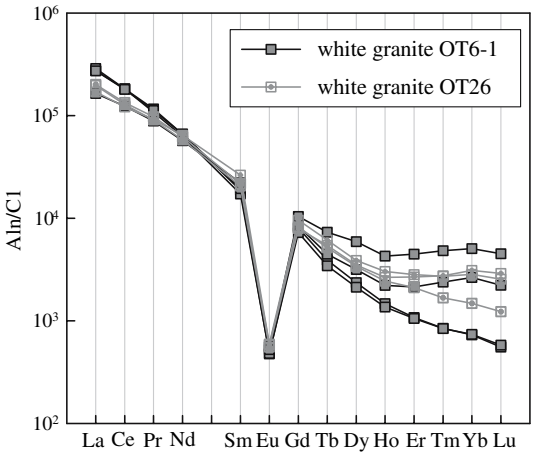

Fig. 8 REE compositions of allanite from *white granite*, normalised to C1 chondrite (Anders and Ebihara 1982)

shows a steady enrichment from LREE to HREE, positive Ce anomaly and a slight negative Eu anomaly. Elongate zircons have highly variable REE concentrations (Table 6) that fluctuate by up to one order of magnitude. The REE pattern of elongate zircons is consistent with those typical of magmatic zircons (Hoskin and Schaltegger 2003). The analyses performed on stubby zircons differ in the unusual

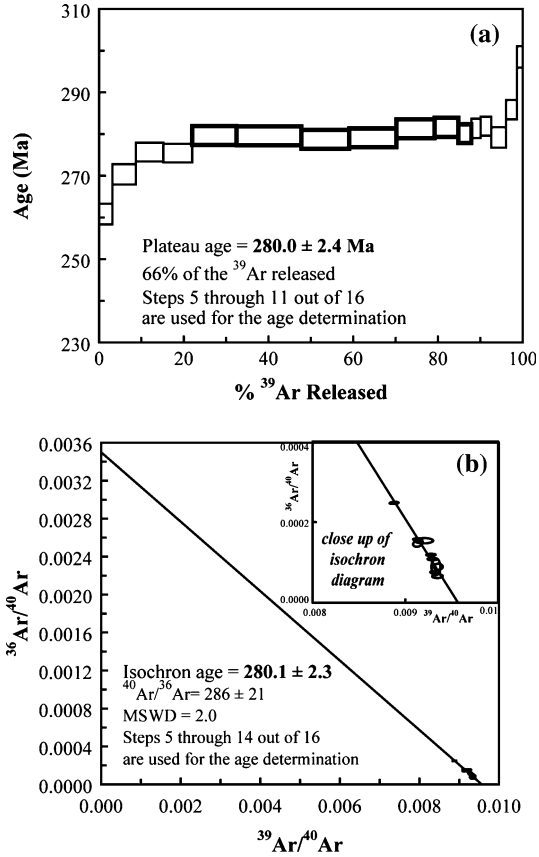

Fig. 9 Age spectrum (a) and isochron (b) diagrams for ^{40}Ar-^{39}Ar incremental heating experiments on hornblende from the trachyandesite dyke (PO1-7). *Error* in the figure are 1σ

LREE enrichment (Table 6; Fig. 11), which is commonly ascribed to partial metamictization (Geisler et al. 2003), thus suggesting that metamict domains are common in this zircon variety.

Twenty-four grains of elongate zircons were dated by LA-ICP-MS (Table 7; Fig. 12a). Ten analyses resulted in concordant ages. Concordant points form a single, well-defined and statistically coherent population that yielded a mean concordia age of 281 ± 3 Ma (2σ, Fig. 12b). The remaining 14 spot analyses are from highly discordant to subconcordant and roughly dispersed along a line parallel to the *x*-axis, which might reflect a common-Pb contribution. A statistically equivalent age (280 ± 4 Ma, 95% confidence interval level) is obtained as lower intercept on a Tera-Wasserburg concordia diagram considering all discordant and concordant data. Four low-luminescent cores were also analysed; two of them yielded a mean concordia age of 278 ± 8 Ma (2σ; Fig. 12c; Table 7). With the exception of two concordant points, analyses from the stubby zircon population yielded discordant and scattered ages (Fig. 12a). This discordance most likely reflects radiogenic Pb loss due to partial metamictization (Mezger

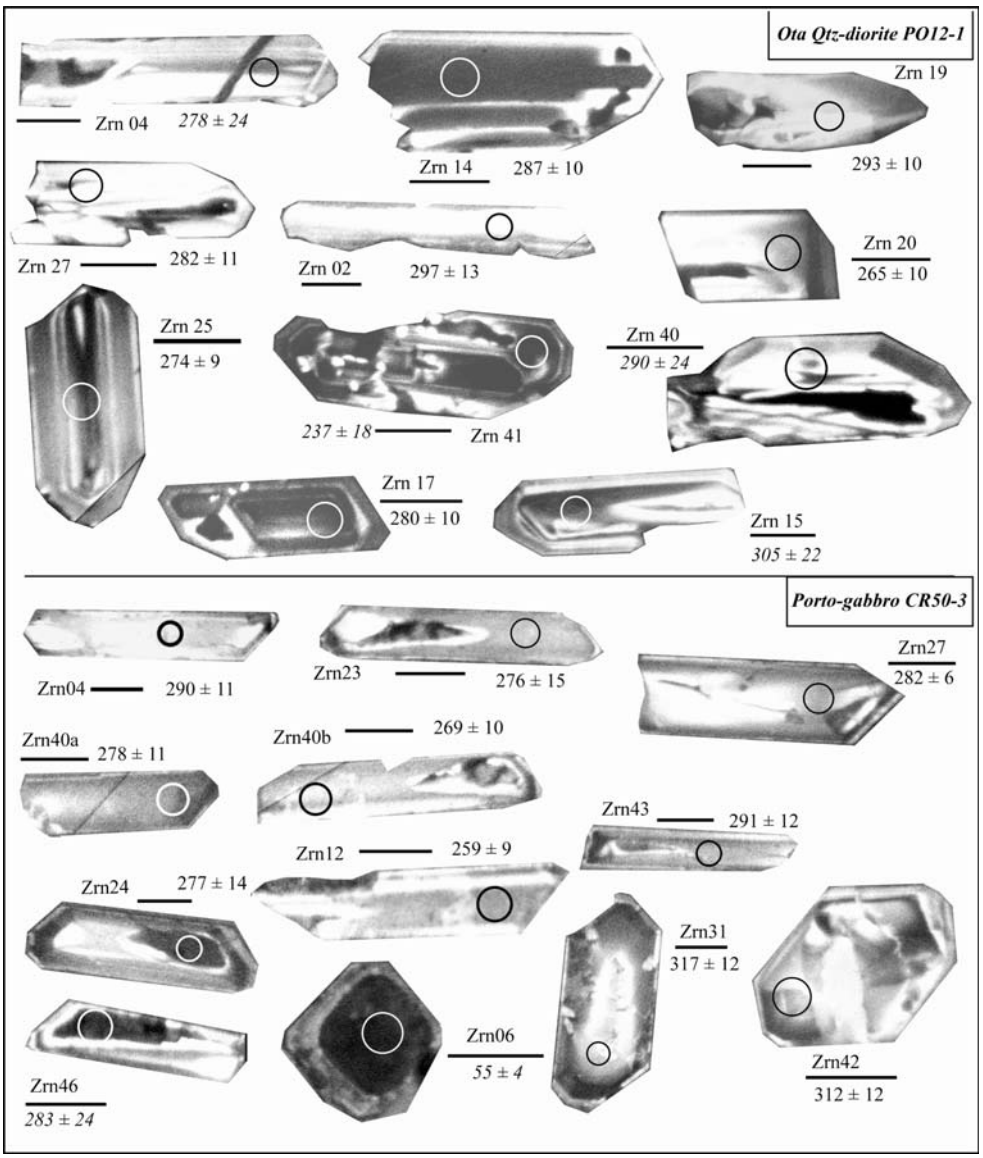

Fig. 10 Main morphologies of zircons from Ota quartz-diorite and Porto-gabbro (cathodoluminescence images); see text and tables for further details. *Scale bars* are 50 μm long. *Circles* correspond to LA-ICP-MS spot. The ages shown in italic character are $^{206}Pb/^{238}U$ ages, those in regular character are concordant ages; the errors are 2σ

and Krogstad 1997), which is in turn suggested by the unusual LREE enrichments. The two concordant points are statistically indistinguishable and yielded a mean concordia age of 276 ± 7 Ma (2σ, Fig. 12c). The significance of different U-Pb zircon ages is discussed after all age data are presented.

Zircon from the Porto-gabbro

Zircons in the selected Porto-gabbro display two main distinct morphologies that resemble those of the zircons in the Ota quartz-diorite. They are mainly elongate needle-shaped and are commonly intensively cracked (Fig. 10). The CL images show that they are faintly zoned or essentially unzoned. Thin low-luminescent cores, with a brighter surface, are locally present and overgrown by a faintly zoned rim in some elongate zircons (e.g. Zrn 24, 46, Fig. 10). A second zircon population, numerically subordinate, consists of larger stubby euhedral zircons that commonly contain apatite grains and dark CL radiation-damaged domains (Fig. 10). Some of these stubby zircons show a bright CL core truncated and overgrown by thin oscillatory zoned rim (e.g. Zrn31 and 42, Fig. 10).

The representative REE composition of elongate and stubby zircons is reported in the incompatible trace element diagram of Fig. 11. The REE pattern of elongate zircon is parallel to that of elongate zircon from the Ota quartz-diorite. It is characterised by an abrupt increase from LREE to HREE (at 0.1–10 and ~10,000 times C1 chondrite, respectively). Ce shows a marked positive anomaly and Eu is depleted relative to neighbouring REE. Similarly to what observed in the Ota quartz-diorite, spot analyses from the stubby zircons of the Porto-gabbro reveal locally an anomalous LREE-enriched pattern relative to elongate

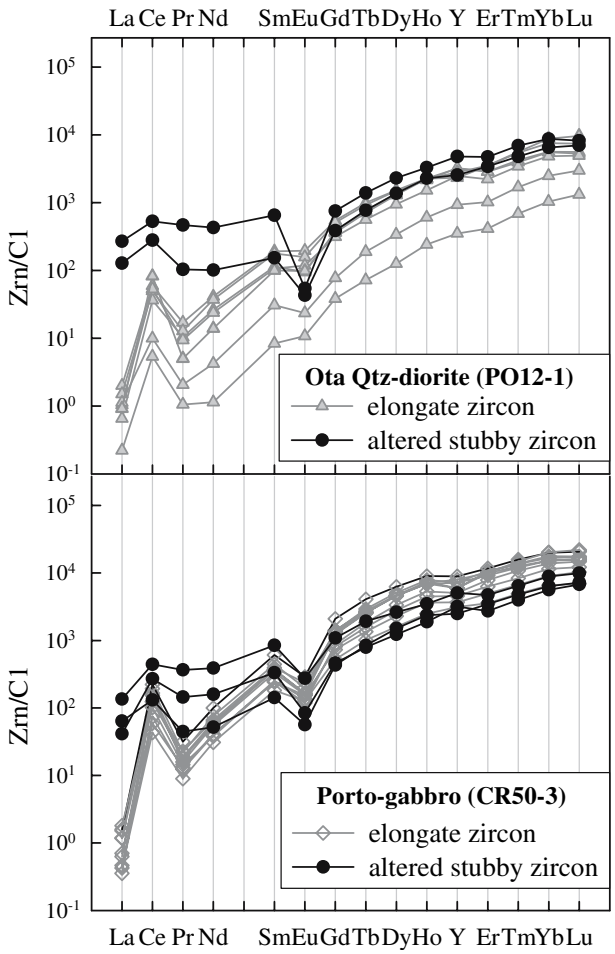

Fig. 11 REE compositions of zircons from Ota quartz-diorite and Porto-gabbro, normalised to C1 chondrite (Anders and Ebihara 1982)

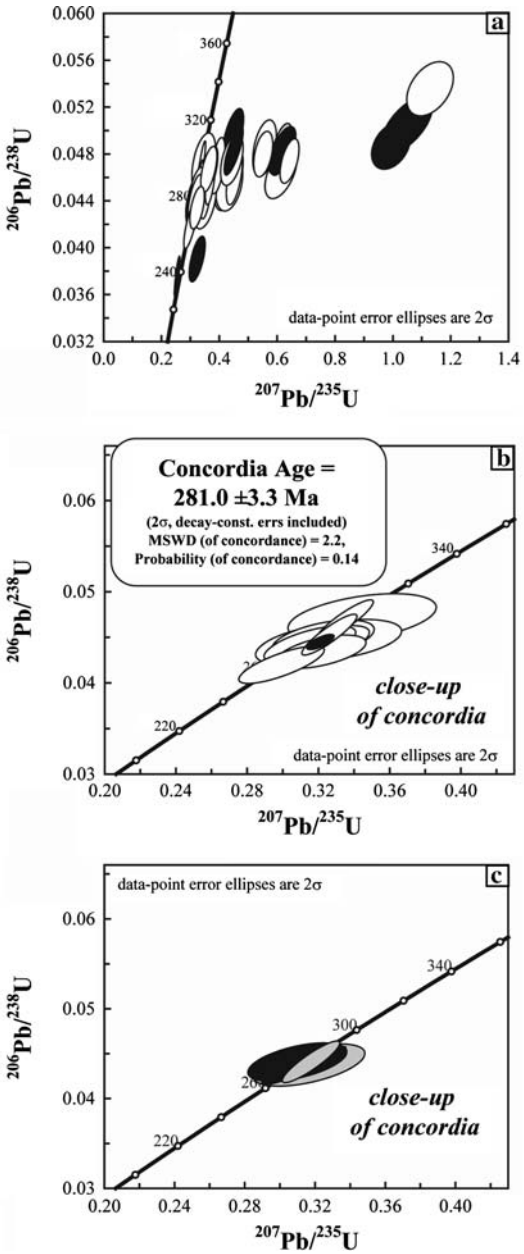

Fig. 12 U-Pb Concordia diagram of zircons from Ota quartz-diorite. Elongate zircons are represented by white ellipses, stubby zircons by black ellipses, low-luminescent cores in elongate zircons by grey ellipses

zircon, thus suggesting that they could have undergone partial metamictization.

Thirty-two grains from the elongate zircon variety were considered for U-Pb isotopic analyses. The U-Pb data exhibit a significant scatter of both discordant and concordant ages (Table 8; Fig. 13a). A single zircon population was provided by 19 concordant points, which yielded a mean concordia age of 283 ± 2 Ma (2σ, Fig. 13b). A slightly younger concordant analysis at 259 ± 9 Ma (2σ) was also identified. Discordant data do not allow in this case to obtain any significant intercept age. Three low-luminescent cores were also dated, one of which yielded a concordia age of 277 ± 14 Ma (2σ; Fig. 13c). Analyses of stubby zircons yielded mostly discordant ages. In particular, two analyses (Zrn6 and 19, Table 8) yielded distinctly younger discordant ages (not reported on the diagram), most likely reflecting isotopic disturbance (Pb loss) due to metamictization, as suggested by the CL image. Two bright CL inherited cores from the stubby variety (grains 31 and 42) were dated and yielded concordia ages at 314 ± 8 Ma (2σ ; Fig. 13c). The significance of zircon ages is reported in the first section of the discussion.

Whole-rock Nd isotope compositions

The initial ε_{Nd} values for the selected samples have been calculated at 282 Ma (Table 9; Fig. 14). The Porto-gabbro and -dolerite have initial ε_{Nd} values of +1.7 and +2.9, respectively. These values are lower than the initial ε_{Nd} of

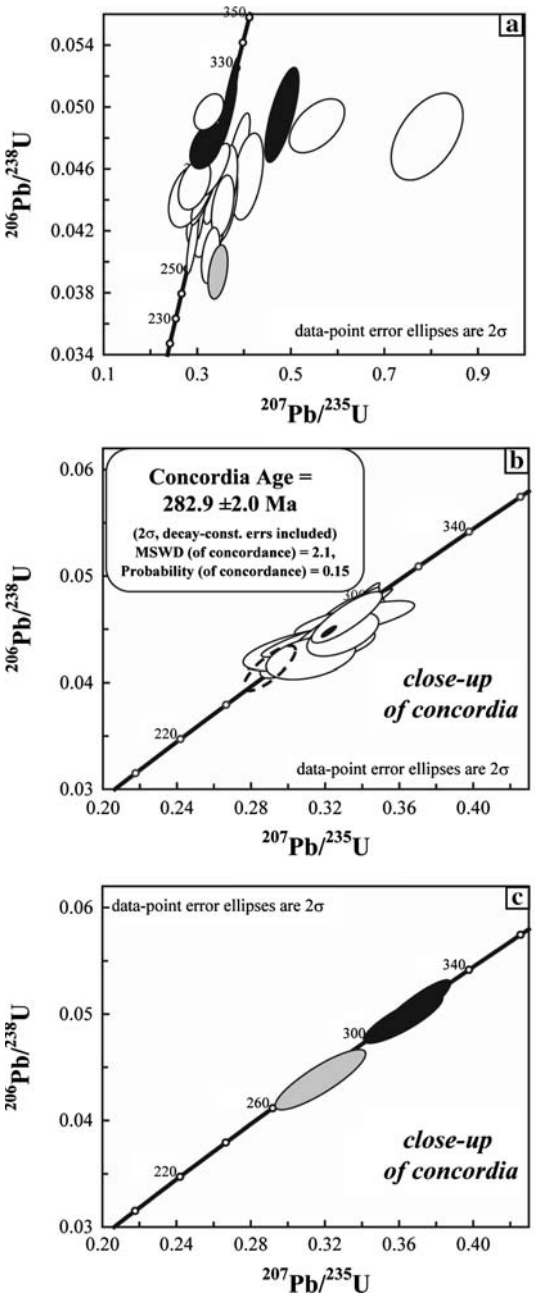

Fig. 13 U-Pb Concordia diagram of zircons from Porto-gabbro. The most discordant analyses (i.e. Zrn6-19) have been omitted from the plot. Elongate zircons are represented by white ellipses, stubby zircons by black ellipses, low-luminescent cores in elongate zircons by grey ellipses. The dashed ellipse corresponds to slightly younger concordant elongate zircon that was not considered for intrusion age calculation (see text for further details)

the Ota olivine-gabbro (+4.9) and are comparable to those of the Ota mafic intrusive sequence (Poitrasson et al. 1995a; Renna et al. 2006). Remarkably, the initial ε_{Nd} of the selected Porto-dolerite is identical to that reported by van Tellingen et al. (1996) for the same rock-type. The trachyandesitic dyke differs from the other mafic rocks in its negative initial ε_{Nd} (–2.0).

The initial ε_{Nd} value of *white granite* OT26 (–0.2) overlaps the values resulting from the analyses carried out by Poitrasson et al. (1995a) and Renna et al. (2006) for the same rock-type (–0.3 to +0.6). The selected *red Calanche granite* has initial ε_{Nd} of +0.9, which is slightly higher than the values based on the investigation by Poitrasson et al. (1995a, –0.1 to 0.0). As a whole, *white* and *red Calanche granites* have initial ε_{Nd} ranging from –0.3 to +0.6 and from –0.1 to +0.9, respectively.

Discussion

Timing of intrusion

Morphology and inner structure similar to those exhibited by elongate zircons in the selected samples are commonly ascribed to rapid growth from a supersaturated melt (Elburg 1996a). This is consistent with the common occurrence of apatite with acicular habit, which is interpreted to develop as a result of the rapid cooling of a basic melt in response to the interaction with an acid magma (Wyllie et al. 1962; Hibbard 1991; Vernon 1991). The elongate zircons from both Ota quartz-diorite and Porto-gabbro should provide crystallisation ages. An elongate zircon from the Porto-gabbro, however, gave a younger U-Pb age [259 ± 9 Ma (2σ)] than the ^{40}Ar-^{39}Ar hornblende age of the crosscutting trachyandesite dyke. Therefore, this young U-Pb zircon age cannot be related to the crystallisation of the mafic intrusives and its nature will be discussed below. The U-Pb ages at 281 ± 3 and 283 ± 2 Ma (2σ) yielded by the remaining elongate zircon fractions of the Ota quartz-diorite and the Porto-gabbro, respectively, therefore most likely represent crystallisation ages.

The age obtained for the Ota quartz-diorite refine the previous K-Ar hornblende and biotite ages of 282 ± 10 Ma provided by Edel et al. (1981) for the mafic rocks of the *Ota association*. The U-Pb zircon age of 281 ± 3 Ma is also in agreement with the K-Ar biotite ages (276 ± 4 and 285 ± 5 Ma) and Rb-Sr whole rock-biotite isochron (287 ± 6 Ma) provided by van Tellingen et al. (1996) for the *white granite*, as field mingling relations point to a coeval crystallisation of the Ota quartz-diorites and the associated biotite granites.

New age constraints on the magmatic activity in the Porto complex are given by the U-Pb zircon age determined for Porto-gabbro and the ^{40}Ar-^{39}Ar hornblende age evaluated for the trachyandesite dyke crosscutting the *red Calanche granite*. The ^{40}Ar-^{39}Ar hornblende age of 280 ± 2 Ma (1σ) is, within error, the same age as the U-Pb zircon

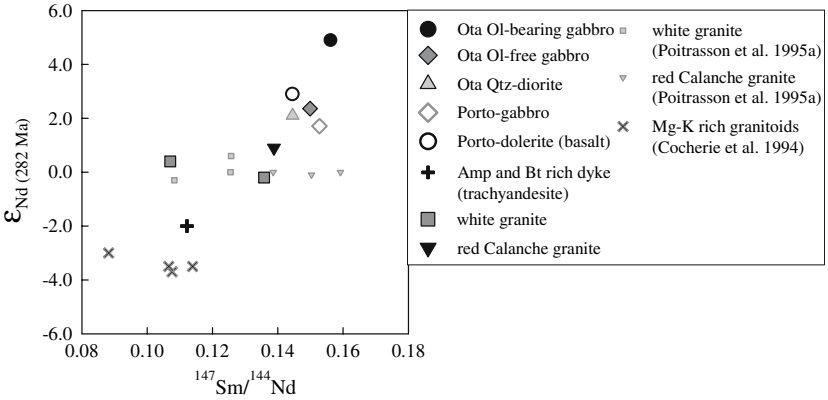

Fig. 14 Plot of ε_{Nd} calculated at 282 Ma (age of emplacement of the Porto complex) versus $^{147}Sm/^{144}Nd$. Data after this work and Renna et al. (2006). Analytical uncertainty for initial ε_{Nd}, obtained after propagation of the uncertainties in $^{147}Sm/^{144}Nd$ and $^{143}Nd/^{144}Nd$ ratios, is within the symbol area. The compositions of *white* and *red Calanche granites* (Poitrasson et al. 1995a) and Mg–K rich granitoids (Cocherie et al. 1994) are also reported

ages of both Porto-gabbro and Ota quartz-diorite. According to field relations the obtained ^{40}Ar-^{39}Ar age implies that the *red Calanche granite* formed prior to 278 Ma, that is earlier than previously determined on the basis of whole-rock Rb-Sr data (van Tellingen et al. 1988). This conclusion is also supported by mingling relations that attest the coeval crystallisation of the *red Calanche granite* and the Porto-gabbro. As a whole, the age of emplacement of the Porto mafic and acid magmas is coeval to the events that led to the intrusion of gabbroic complexes and related dykes, and of A-type granites in the Corsica batholith (~285 Ma; Paquette et al. 2003; Cocherie et al. 2005).

Origin of stubby zircons

The common disturbance of the U-Pb system in stubby zircons hampers to draw robust conclusions about the age and the origin of stubby zircon population. The only two concordant stubby zircons (showing oscillatory zoning indicative of their magmatic origin) from the Ota quartz-diorite give an age of 276 ± 7 Ma (2σ), which is statistically equivalent to the crystallisation age inferred for the same sample. Similar ages have been determined for the low-luminescent cores within elongate zircons from both Ota quartz-diorite and Porto-gabbro, which yielded a mean age of 278 ± 8 Ma (2σ) and 277 ± 14 Ma (2σ), respectively.

Two hypotheses may be formulated for the origin of stubby zircons and low-luminescent cores in elongate zircons. In the first, they crystallised from the basic magma, before the interaction with the acid magma that gave rise to the associated biotite granites. The second hypothesis implies a xenocrystic origin. In particular, stubby zircons in mafic rocks resemble morphology, inner structure, trace element signature and strong degree of discordance shown by Porto granite zircons (Renna 2004). We thus favour the latter interpretation, which implies that such xenocrystic component was entrained from the acid magma during mingling processes.

An older inherited component is revealed by the U-Pb zircon age of 314 ± 8 Ma yielded by the cores of stubby zircons from the Porto-gabbro. This age is consistent with that inferred for some of the calc-alkaline plutons enclosing the Porto complex (Paquette et al. 2003). Following the above interpretation, for the origin of stubby zircons and low-luminescent cores in elongate zircons, such an older component was likely assimilated by the acid magma.

Post-magmatic evolution

One zircon from the Porto-gabbro gave a U-Pb age of 259 ± 9 Ma. This age is younger than that of the crosscutting trachyandesite dyke (280 ± 2 Ma) and thus cannot be related to the crystallisation of the gabbro. However, the young zircon does not show clear differences in CL images relative to the other elongate zircon grains from the same gabbro sample. In addition, this zircon has a fine size, thus preventing to obtain trace element analyses on the same grain, which could provide additional information on its origin. It is thus not straightforward to establish the significance of the U-Pb zircon age of 259 ± 9 Ma.

The red Calanche granite, which displays mingling relations with the Porto-gabbro, gave an imprecise whole-rock Rb-Sr isochron with a similar age (251 ± 14 Ma, van Tellingen et al. 1988). This isochron could reflect a perturbation of the Rb-Sr isotope system during a late hydrothermal event, which was documented by Poitrasson et al. (1995b) on the basis of REE and Nd isotope investigations. In particular, it was shown that the interaction with hydrothermal fluids, highlighted by the common occurrence of miarolitic cavities, locally modified the Nd isotope signature of the red Calanche granite (Poitrasson et al. 1995b). This hydrothermal event most likely reset the initial $^{87}Sr/^{86}Sr$ values, thus resulting in the Rb-Sr whole-rock isochron (van Tellingen et al. 1988). Remarkably, the high sensitivity of Rb-Sr isotope system to post-magmatic alteration for other A-type Corsican granites was already shown by Poitrasson et al. (1995a).

This suggests a reliable geological significance to the young U-Pb zircon age, as the U-Pb isotope system in zircon may be affected by hydrothermal circulation (Rubin et al. 1989; Claouè-Long et al. 1990; Sinha et al. 1992; Wayne and Sinha 1992). In particular, the occurrence of partially metamict zircons in the Porto-intrusive rocks (Renna 2004) leads us to consider that the young zircon could be partially metamict and reset by the circulations of fluids related to the hydrothermal event recognised (Poitrasson et al. 1995b) for the *red Calanche granite*. Metamict zircon, with its disordered lattice, tends to recrystallise, even under low temperature conditions (~200°C; Geisler et al. 2003 and references therein). This process is commonly associated with important loss and/or exchange of lead with their environment (Krogh and Davis 1975; Gebauer and Grunenfelder 1976). We thus propose that the young U-Pb zircon age dates the hydrothermal circulation that affected the Porto gabbro-granite complex, at 10–35 Ma after its emplacement.

Inferences on the origin and evolution of the Porto-gabbro and mafic dykes

Renna et al. (2006) showed on the basis of trace element and Nd isotope data that Ota parental basic melts were derived from a depleted mantle source, and evolved through a process of fractional crystallisation and concomitant crustal contamination. In particular, the decrease of initial ε_{Nd} and the increase of Th and U concentrations, from olivine-gabbro to olivine-free gabbro and quartz-diorite, were attributed to a process of contamination by the acid magma corresponding to the associated *white granites*.

The Porto-gabbro and the mafic dykes share most of the whole-rock major, trace element and Nd-isotope characteristics of Ota mafic intrusive rocks (Table 1; Figs. 3, 14), thus suggesting that they formed from parental basic melts with similar compositions. The similarities of trace element compositions (Table 2; Fig. 6) between the clinopyroxenes from the Porto-gabbro and -dolerite and that of Ota counterparts (Renna et al. 2006) are also consistent with this interpretation. Minor geochemical differences, however, indicate that the Porto-gabbro and mafic dykes parental melts experienced distinct evolutionary histories.

A low extent of fractional crystallisation (mainly controlled by plagioclase and clinopyroxene segregation) may explain the lower Mg#, CaO and higher TiO_2, MnO and REE contents of the Porto-gabbro relative to Ota gabbros (Table 1). A significant crustal contamination of the melt that gave rise to the Porto-gabbro parental melts cannot be discarded, as for instance indicated by the occurrence of inherited zircons, assimilated by the associated acid magma, and by its lower initial ε_{Nd} relative to Ota olivine-gabbro (+1.7 and +4.9, respectively). Remarkably, the variable U and Th enrichments in clinopyroxene from the Porto-gabbro fit well with a process of contamination by the acid magma corresponding to the associated *red Calanche granite*, which has high U and Th concentrations (Table 1).

The occurrence of a negative Eu anomaly in the REE pattern of mafic dykes (Fig. 3) suggest that their parental melts have undergone an early fractional crystallisation process controlled by plagioclase segregation. The lower initial ε_{Nd} shown by the Porto-dolerite relative to Ota olivine-gabbro (+2.9 and +4.9, respectively) makes it likely that the Porto-dolerite was also affected by crustal contamination. A contamination process in the igneous evolution of Porto-dolerite parental melt is consistent with the local occurrence of K-feldspar-rich veins within the external portion of the dyke, which most likely represent late and local magmatic injections segregated out of the almost solidified, host acid magma. However, clinopyroxene from the Porto-dolerite does not record this contamination event. In particular, it does not display a significant enrichment in Th and U, as observed in the evolved rocks of the Ota mafic sequence (Renna et al. 2006) and Porto-gabbro. Clinopyroxene trace element signature thus contrasts with the inference given by the whole-rock initial ε_{Nd} value. As a whole, these data could indicate that parental melts feeding the different mafic intrusive bodies and basic dykes of the Porto complex were derived from a mantle source with a slightly heterogeneous Nd isotope composition. Alternatively, the crustal material that contaminated the melt feeding the Porto-dolerite, possibly at a deeper magma chamber, was poor in Th and U.

The Ota-dyke records a significant amount of crustal contamination, most likely by acid material, as shown by the occurrence of quartz ocelli. Such a process could have been responsible for the higher Rb, Th, U and Pb of the Ota-dyke relative to the Porto-dolerite and Ota gabbros (Table 1).

Origin of the trachyandesite dyke

An accurate determination of trachyandesite dyke parental melt compositions is hampered by the fact that it corresponds to a highly evolved melt. The trachyandesite and mafic dykes may derive from parental melts with similar compositions. Nonetheless, the trachyandesite dyke has significant geochemical differences relative to the mafic dykes. In particular, it differs in the higher concentrations of Rb, Ba, K, Th, LREE, and in the lower contents of Y, HREE and initial ε_{Nd} value.

The trace element and isotopic signature of the trachyandesite might be related to a basic melt that underwent an extensive evolution controlled by both fractional crystallisation and assimilation of crustal material. Remarkably,

most of the geochemical features of the Mg–K rich granitoids, which represent the host rock of the Porto complex (Carmignani et al. 2000), parallel those displayed by the trachyandesite dyke. In particular, the Mg–K rich granitoids from the Corsica batholith have extremely high contents of Rb, K, Ba, Th and LREE (Cocherie et al. 1994). This suggests that the Mg–K rich granitoids represent the dominant contaminant component of the trachyandesite parental melt. This hypothesis is confirmed by the Nd isotope composition of the Mg–K rich granitoids (Cocherie et al. 1994) at the time of the emplacement of the Porto complex, which are in agreement with the enriched Nd isotope signature of the trachyandesite dyke (Fig. 14).

The geochemical patterns resulting from addition to the basalt magma of contaminants are complex (e.g. Patchett 1980; Elburg 1996b). Nonetheless, the initial ε_{Nd} value of the trachyandesite indicates an extreme contamination by crustal material. A rough assessment of the crustal contribution in the origin of the trachyandesite parental melt was carried out through a simple two-component model. The average Nd isotope composition of Mg–K rich granitoids at the time of the emplacement of the Porto complex (ε_{Nd} = –3.4, Cocherie et al. 1994) was assumed as representative of the crustal contaminant. We have also considered that the initial Nd isotope composition of the Ota olivine-gabbro (the least evolved mafic rock, with initial ε_{Nd} = + 4.9) represents the isotope composition of the parental mantle-derived melt. The initial ε_{Nd} value of the trachyandesite was reproduced with 83 wt% fraction of exotic component.

Origin of biotite granites

Most chemical variations among the different granite types may be related to a geochemical evolution controlled by a process of fractional crystallisation. This is for instance indicated by the increasing Rb/Sr ratio from the *white* to the *red Calanche granite*, which is in the ranges 1.65–4.2 and 23–33, respectively. In addition, the decrease of CaO, K_2O, Ba, Sr, associated with an increasing magnitude of the negative Eu anomaly from the *white* to the *red Calanche granite*, is consistent with the removal of feldspars (Table 1, Fig. 4). The decrease of Fe, Mg and Ti should reflect the separation of biotite and Fe–Ti oxide phases. However, the LREE decrease from the *white* to the *red Calanche granite*, which is associated with an increase of HREE concentrations (Fig. 4), can be achieved only by involving allanite in the fractionating assemblage. The segregation of this LREE-rich phase (Fig. 8) produces a decrease of LREE concentrations in the residual melts with increasing crystallisation index (Fourcade and Allègre 1981; Miller and Mittlefehldt 1982; Gromet and Silver 1983). Remarkably, the plagioclase zoning within the *white granites* (outward decrease of LREE, Eu, Sr and Ba) parallels the compositional variations observed for the whole-rock chemical variations from white to red granites, thus reinforcing a genetic link trough fractional crystallisation. A similar igneous evolution trough fractional crystallisation of feldspars and minor allanite was also proposed for the coeval A-type subsolvus granite of Tana Peloso (Poitrasson et al. 1994). The inferred coeval emplacement and absence of significant variations in the initial Nd isotope composition (Fig. 14) between the *white* and the *red Calanche granite* (see also Poitrasson et al. 1995a) is consistent with a formation by a common parental melt. As a whole, the limited range in initial ε_{Nd} of the biotite granites (–0.3 to +0.9) could be related to the local dispersion of a basic component (Renna et al. 2006) and late hydrothermal alteration (Poitrasson et al. 1995b).

Poitrasson et al. (1995a) proposed two different source materials for the origin of metaluminous to mildly peraluminous A-type granites of the Corsica batholith. The parental melts of the A-type granites developed from partial melting of lower-crustal mafic reservoirs, as indicated for the aluminous subsolvus granites, or mantle sources that gave rise to basic melts whose evolution comprised a substantial assimilation of crustal material. The latter origin was specifically proposed for the aluminous hypersolvus granites (Poitrasson et al. 1995a). The new data of the present work indicate that the Porto *white* and *red Calanche granites* were derived from a common parental melt, but we have no clear arguments for determining the source material of their parental melts. Remarkably, the Porto biotite granites share many geochemical similarities with coeval and volumetrically abundant aluminous subsolvus granites from the Corsica batholith (i.e. Tana-Peloso, Cauro-Bastelica, Mizane and Pastricciola; Poitrasson et al. 1994, 1995a). The hypothesis that these granites were purely mantle-derived seems unlikely, as large volumes of basic melts are required. Therefore, a dominant component derived from the lower continental crust is favoured for the parental melts that gave rise to the Porto biotite granites. High heat input from rising asthenospheric mantle, as revealed by the coeval lower crust intrusion of MORB-type magmas (Voshage et al. 1990; Hermann et al. 2001; Montanini and Tribuzio 2001; Paquette et al. 2003), could have favoured the generation of the subsolvus aluminous A-type granites (see also Poitrasson et al. 1994, 1995a).

Conclusions

The post-Variscan complex of Porto comprises a bimodal magmatic association of metaluminous to slightly peraluminous A-type biotite granites mingled with mafic intrusives, emplaced at shallow crustal levels and crosscut

by basic to intermediate dykes. The complex formed by repeated injections of basic melts intruding a crystallizing acid magma. The latter essentially evolved by fractional crystallisation, controlled by separation of feldspars and minor allanite. The last basic melt pulses occurred when the granite sequence was completely solidified. Mafic intrusives have been dated at 281 ± 3 and 283 ± 2 Ma. A late dyke yielded an age of 280 ± 2 Ma, thus implying that the whole evolution occurred in a short time span. The parental basic melts had a similar trace element fingerprint and were derived from an isotopically depleted, most likely asthenospheric, mantle source. Minor chemical variations observed for the mafic rocks are probably due to slightly different evolutionary histories, which are indeed controlled by fractional crystallisation and crustal contamination. The latter mostly occurred through assimilation of the acid magma corresponding to the associated biotite granites. The older calc-alkaline Variscan plutons could also have played a significant role in the crustal contamination of the basic melts. A U-Pb zircon age of 259 ± 9 Ma probably dates an hydrothermal event that affected the Porto complex after its emplacement.

Acknowledgments G. De Grandis (CNR-IGG, Unità di Pisa) and A. Borghi (Dipartimento di Scienze Mineralogiche e Petrologiche, Università di Torino) are thanked for their help with zircon separation and CL imaging, respectively. We are grateful to M. Elburg and F. Poitrasson for their constructive reviews. This work was supported by Ministero dell'Università e della Ricerca Scientifica (Progetti di Ricerca di Interesse Nazionale), Università di Pavia (Fondi di Ateneo per la Ricerca) and Consiglio Nazionale delle Ricerche (C.N.R.) funds. The P.N.R.A. has supported the purchase of the laser probe and of the mass spectrometer.

References

Anders E, Ebihara M (1982) Solar system abundances of the elements. Geochim Cosmochim Acta 46:2363–2380

Barker DS (1970) Compositions of granophyre, myrmekite, and graphic granite. Geol Soc Am Bull 81:3339–3350

Bennett EH (1980) Granitic rocks of tertiary age in the idaho batholith and their relation to mineralization. Econ Geol 75:278–288

Bennett EH, Knowles CR (1983) Tertiary plutons and related rocks in central Idaho. US Geol Surv Bull 1658:81–95

Blichert-Toft J, Rosing MT, Lesher CE, Chauvel C (1995) Geochemical constraints on the origin of the late Archean Skjoldungen alkaline igneous province, SE Greenland. J Petrol 36:515–561

Bonin B (1988) Peralkaline granites of Corsica: some petrological and geochemical constraints. Rend Soc Ital Min Petrol 43:281–306

Carmignani L, Rossi P, Barca S, Durand-Delga M, Lahondere D, Oggiano G, Salvatori I, Conti P, Eltrudis J, Funedda A, Pasci S, Cerchi GP, Disperati L, Ferrandini J, Loye-Pilot MD, Sartia E, Spano C (2000) Carta geologica e strutturale della Sardegna e della Corsica, scala 1/500000. Servizio geologico d'Italia, Regione Sardegna, BRGM, Collectivité Territoriale de Corse

Cavazza W, Zattin M, Ventura B, Zuffa GG (2001) Apatite fission-track analysis of Neogene exhumation in northern Corsica (France). Terra Nova 13:51–57

Cebula GT, Kunk MJ, Mehnert HH, Naeser CW, Obradovich JD, Sutter JF (1986) The Fish Canyon Tuff, a potential standard for the ^{40}Ar-^{39}Ar and fission-track dating methods (abstract). Terra Cognita (6th Int. Conf. on Geochronology, Cosmochronology and Isotope Geology) 6:139

Claoué-Long JC, King RW, Kerrich R (1990) Archean hydrothermal zircon in the Abitibi greenstone belt: constraints on the timing of gold mineralisation. Earth Planet Sci Lett 98:109–128

Cocherie A, Rossi P, Fouillac AM and Vidal P (1994) Crust and mantle contributions to granite genesis—an example from the Variscan batholith of Corsica, France, studied by trace element and Nd-Sr-O isotope systematics. Chem Geol 115:173–211

Cocherie A, Rossi P, Fanning CM, Guerrot C (2005) Comparative use of TIMS and SHRIMP for U-Pb zircon dating and mafic tholeiitic layered complexes and dykes from the Corsican Batholith (France). Lithos 82:185–219

Corfu F, Hanchar JM, Hoskin PWO, Kinny P (2003) Atlas of zircon textures. In: Hanchar JM and Hoskin PWO (eds) Zircon, vol 53. Mineralogical Society of America, Washington, pp 468–500

Edel JB, Montigny R, Thuizat R (1981) Late Paleozoic rotations of Corsica and Sardinia: new evidence from paleomagnetic and K-Ar studies. Tectonophysics 79:201–223

Elburg MA (1996a) U-Pb ages and morphologies of zircon in micrograniteoid enclaves and peraluminous host granite: evidence for magma mingling. Contrib Mineral Petrol 123:177–189

Elburg MA (1996b) Evidence of isotopic equilibration between micrograniteoid enclaves and host granodiorite, Warburton Granodiorite, Lachlan Fold Belt, Australia. Lithos 38:1–22

Fellin MG, Picotti V, Zattin M (2005) Neogene to quaternary rifting and inversion in Corsica: retreat and collision in western Mediterranean. Tectonics 24:TC1011. doi:10.1029/2003TC001613

Ferré EC, Leake B (2001) Geodynamic significance of early orogenic high-K crustal and mantle melts: example of the Corsica Batholith. Lithos 59:47–67

Fourcade S, Allègre CJ (1981) Trace element behaviour in granite genesis-a case study: the calc-alkaline plutonism association from the Querigut complex (Pyrénées, France). Contrib Mineral Petrol 76:177–195

Gebauer D, Grunenfelder M (1976) U-Pb and Rb-Sr whole-rock dating of low-grade metasediments. Example: Montagne Noire (Southern France). Contrib Mineral Petrol 59:13–32

Geisler T, Rashwan AA, Rahn MKW, Poller U, Zwingmann H, Pidgeon RT, Schleicher H, Tomaschek F (2003) Low-temperature hydrothermal alteration of natural metamict zircons from the Eastern Desert, Egypt. Mineral Magaz 67(3):485–508

Gromet LP, Silver LT (1983) Rare earth element distribution among minerals in a granodiorite and their petrogenetic implications. Geochim Cosmochim Acta 47:925–939

Hermann J, Müntener O, Günther D (2001) Differentiation of mafic magma in a continental crust-to-mantle transition zone. J Petrol 42:189–206

Hibbard MJ (1991) Textural anatomy of twelve magma-mixed granitoid systems. In: Didier J, Barbarin B (eds) Enclaves and granite petrology. Elsevier, Amsterdam, pp 431–444

Horstwood MSA, Foster GL, Parrish RR, Noble SR, Nowell GM (2003) Common-Pb corrected in situ U-Pb accessory mineral geochronology by LA-MC-ICP-MS. J Anal At Spectrom 18:837–846

Hoskin PWO, Schaltegger U (2003) The composition of zircon in igneous and metamorphic petrogenesis. In: Hanchar JM, Hoskin PWO (eds) Zircon, vol 53. Mineralogical Society of America, Washington, pp 27–62

Ketchum JWF, Jackson SE, Culshaw NG, Barr SM (2001) Depositional and tectonic setting of the Paleoproterozoic Lower Aillik Group, Makkovik Province, Canada: evolution of a passive margin—foredeep sequence based on petrochemistry and U-Pb (TIMS and LAM-ICP-MS) geochronology. Precambrian Res 105:331–356

Krogh TE, Davis GL (1975) Alteration in zircons and differential dissolution of altered and metamict zircons. Carnegie Institution of Washington Yearbook, pp 619–623

Le Maitre RW (1989) A classification of igneous rocks and glossary of terms. Blackwell, Oxford

Lewis RS e Kilsgaard TH (1991) Eocene plutonic rocks in south central Idaho. J Geophys Res 96:295–311

Ludwig KR (2003) ISOPLOT 3.00: a geochronological toolkit for microsoft excel. Berkeley Geochronology Center, Berkeley

Mezger K, Krogstad EJ (1997) Interpretation of discordant U-Pb zircon ages: an evaluation. J Metamorphic Geol 15:127–140

Miller CF, Mittlefehldt DW (1982) Light rare earth element depletion in felsic magmas. Geology 10:129–133

Montanini A, Tribuzio R (2001) Gabbro-derived granulites from the Northern Apennines (Italy): evidence for lower-crustal emplacement of tholeiitic liquids in post-Variscan times. J Petrol 42:2259–2277

Paquette JL, Ménot RP, Pin C, Orsini JB (2003) Episodic and short-lived granitic pulses in a post-collisional setting: evidence from precise U-Pb zircon dating through a crustal cross-section in Corsica. Chem Geol 198:1–20

Patchett PJ (1980) Thermal effects of basalt on continental crust and crustal contamination of magmas. Nature 283(7):559–561

Platevoet B, Bonin B (1991) Enclaves and mafic-felsic associations in the Permian alkaline province of Corsica, France: Physical and chemical interactions between coeval magmas. In: Didier J, Barbarin B (eds) Enclaves and granite petrology. Elsevier, Amsterdam, pp 263–275

Platevoet B, Bonin B, Pupin JP, Gondolo A (1988) Les associations acide-basique du magmatisme alcalin anorogénique de Corse. Bull Soc géol France 8:43–55

Poitrasson F (2002) In situ investigations of allanite hydrothermal alteration: examples from calc-alkaline and anorogenic granites of Corsica (southeast France). Contrib Mineral Petrol 142:485–500

Poitrasson F, Pin C, Duthou JL, Platevoet B (1994) Aluminous subsolvus anorogenic granite genesis in the light of Nd isotopic heterogeneity. Chem Geol 112:199–219

Poitrasson F, Duthou JL, Pin C (1995a) The relationship between petrology and Nd isotopes as evidence for contrasting anorogenic granite genesis: example of the Corsican Province (SE France). J Petrol 36:1251–1274

Poitrasson F, Pin C, Duthou JL (1995b) Hydrothermal remobilization of rare earth elements and its effect on Nd isotopes in rhyolite and granite. Earth Planet Sci Lett 130:1–11

Reiners PW, Spell TL, Nicolescu S, Zanetti KA (2004) Zircon (U-Th)/He thermochronometry: He diffusion and comparisons with $^{40}Ar/^{39}Ar$ dating. Geochim Cosmochim Acta 68:1857–1887

Renna MR (2004) Petrologia e geocronologia U-Pb del complesso di Porto (Corsica Nord-Occidentale). PhD Thesis, Università di Pavia

Renna MR, Tribuzio R, Tiepolo M (2006) Interaction between basic and acid magmas during the latest stages of the post-collisional Variscan evolution: clues from the gabbro-granite association of Ota (Corsica-Sardinia batholith). Lithos 90:92–110

Rubin JN, Henry CD, Price JG (1989) Hydrothermal zircons and zircon overgrowths, Sierra Blanca Peaks, Texas. Am Mineral 74:865–869

Sinha AK, Wayne DM, Hewitt DA (1992) The hydrothermal stability of zircon: preliminary experimental and isotopic studies. Geochim Cosmochim Acta 56:3551–3560

Staudacher TH, Jessberger EK, Dorflinger D, Kiko J (1978) A refined ultrahigh-vacuum furnace for rare gas analysis. J Phys E Sci Instrum 11:781–784

Steven TA, Mehnert HH, Obradovich JD (1967) Age of volcanic activity in the San Juan Mountains, Colorado. U S Geol Surv Prof Pap 575-D:47–55

Tiepolo M (2003) Pb geochronology of zircon with laser ablation—inductively coupled plasma—mass spectrometry. Chem Geol 199:159–177

Tiepolo M, Bottazzi P, Palenzona M, Vannucci R (2003) A laser probe coupled with ICP-Double-Focusing Sector-Field Mass Spectrometer for in situ analysis of geological samples and U-Pb dating of zircon. Can Mineral 41:259–272

Tommasini S, Poli G, Halliday AN (1995) The role of sediment subduction and crustal growth in the Hercynian plutonism: isotopic and trace element evidence from the Sardinia-Corsica batholith. J Petrol 36:1305–1332

van Tellingen HW (1955) Géologie et pétrologie de la région de Port (Corse). PhD Thesis of the Universiteit van Amsterdam

van Tellingen HW, Verschure R, Andriessen P (1988) Note on radiometric age determinations of two granites from western Corsica: the white granite of the Ota association and the red Calanche granite. Bull Soc Géol France 8:973–977

van Tellingen HW, Verschure RH, Andriessen PAM (1996) Indications for an early Miocene mafic dyke swarm in western Corsica. A combined fission track, isotopic and geochemical investigation. Proc Kon Ned Akad v Wetensch 99(1–2):85–104

Vellutini P (1975) Sur la structure du massif du granite rouge de Porto (Corse du Nord-Ouest). Comptes Rendus Acad Sci Paris, Ser. II 280:813–815

Vernon RH (1991) Interpretation of microstructures of microgranitoid enclaves. In: Didier J and Barbarin B (eds) Enclaves and granite petrology. Elsevier, Amsterdam, pp 277–291

Voshage H, Hofmann AW, Mazzucchelli M, Rivalenti G, Sinigoi S, Raczek I, Demarchi G (1990) Isotopic evidence from the Ivrea Zone for a hybrid lower crust formed by magmatic underplating. Nature 347:731–736

Wayne DM, Sinha AK (1992) Stability of zircon U-Pb systematics in a greenschist-grade mylonite: an example from the Rockfish Valley fault zone, central Virginia, USA. J Geol 100:593–603

Whalen JB, Currie KL and Chappell BW (1987) A-type granites: geochemical characteristics, discrimination and petrogenesis. Contrib Mineral Petrol 95:407–419

Wiedenbeck M, Alle P, Corfu F, Griffin WL, Meier M, Oberli F, Von Quadt A, Roddick JC, Spiegel W (1995) Three natural zircon standards for U-Th-Pb, Lu-Hf, trace elements ad REE analyses. Geostand Newsl 19:1–23

Wyllie PJ, Cox KG, Biggar GM (1962) The habit of apatite in synthetic systems and igneous rocks. J Petrol 3:238–243

Zarki-Janki B, van der Beek P, Popeau G, Sosson M, Rossi P, Ferrandini J (2004) Cenozoic denudation of Corsica in response to Ligurian and Thyrrenian extension: results from apatite fission track thermochronology. Tectonics 23:TC1003. doi:10.1029/2003TC001535